INVESTIGATION OF ROTOR WAKE INTERACTIONS IN HELICOPTERS USING 3D UNSTEADY FREE VORTEX WAKE METHODOLOGY

A THESIS SUBMITTED TO
THE GRADUATE SCHOOL OF NATURAL AND APPLIED SCIENCES
OF
MIDDLE EAST TECHNICAL UNIVERSITY

BY

ÖZNUR YEMENİCİ

IN PARTIAL FULFILLMENT OF THE REQUIREMENTS
FOR
THE DEGREE OF MASTER OF SCIENCE
IN
AEROSPACE ENGINEERING

DECEMBER 2009

Approval of the thesis:

INVESTIGATION OF ROTOR WAKE INTERACTIONS IN HELICOPTERS USING 3D UNSTEADY FREE VORTEX WAKE METHODOLOGY

submitted by **ÖZNUR YEMENİCİ** in partial fulfillment of the requirements for the degree of **Master of Science in Aerospace Engineering Department, Middle East Technical University** by,

Prof. Dr. Canan Özgen _____
Dean, Graduate School of **Natural and Applied Sciences**

Prof. Dr. Ozan Tekinalp _____
Head of Department, **Aerospace Engineering**

Asst. Prof. Dr. Oğuz Uzol _____
Supervisor, **Aerospace Engineering Dept., METU**

Asst. Prof. Dr. Nilay Sezer Uzol _____
Co-Supervisor, **Mechanical Engineering Dept.,**
TOBB University of Economics and Technology

Examining Committee Members:

Prof. Dr. Cahit Çıray _____
Aerospace Engineering Dept., METU

Asst. Prof. Dr. Oğuz Uzol _____
Aerospace Engineering Dept., METU

Prof. Dr. Ünver Kaynak
Mechanical Engineering Dept., _____
TOBB University of Economics and Technology

Asst. Prof. Dr. İlkay Yavrucuk _____
Aerospace Engineering Dept., METU

Asst. Prof. Dr. Güçlü Seber _____
Aerospace Engineering Dept., METU

Date:

I hereby declare that all information in this document has been obtained and presented in accordance with academic rules and ethical conduct. I also declare that, as required by these rules and conduct, I have fully cited and referenced all material and results that are not original to this work.

Name, Last Name: Öznur YEMENİCİ

Signature:

ABSTRACT

INVESTIGATION OF ROTOR WAKE INTERACTIONS IN HELICOPTERS USING 3D UNSTEADY FREE VORTEX WAKE METHODOLOGY

Yemenici, Öznur

M.S., Department of Aerospace Engineering

Supervisor: Asst. Prof. Dr. Oğuz Uzol

Co-Supervisor: Asst. Prof. Dr. Nilay Sezer Uzol

December 2009, 78 pages

This thesis focuses on developing and examining the capabilities of a new in-house aerodynamic analysis tool, AeroSIM+, and investigating rotor-rotor aerodynamic interactions for two helicopters, one behind the other in forward flight. AeroSIM+ is a 3-D unsteady vortex panel method potential flow solver based on a free vortex wake methodology. Validation of the results with the experimental data is performed using the Caradonna-Tung hovering rotor test case. AeroSIM+ code is improved for forward flight conditions so that, the blades are allowed to move according to the rotor dynamics. In the simulations, blade airload prediction is seen to be sensitive to changes in vortex core size. Blade Vortex Interaction (BVI) locations differ depending on the relative position of the rear rotor with respect to the front rotor as well as on the forward flight speed. It was observed that the performance characteristics of the rear rotor alter depending on the relative positions of the rotors within the asymmetric wake flow field. The results of this thesis study such as the computed forces and moments on each rotor and the frequency characteristics of these loads can be also used in helicopter dynamics simulators.

Keywords: helicopter, free wake, aerodynamic interaction

ÖZ

ÜÇ BOYUTLU ZAMANA BAĞLI SERBEST İZ BÖLGESİ MODELLEMESİ İLE ROTOR AERODİNAMİK ETKİLEŞİMLERİNİN İNCELENMESİ

Yemenici, Öznur
Yüksek Lisans, Havacılık ve Uzay Mühendisliği Bölümü
Tez Yöneticisi: Yard. Doç. Dr. Oğuz Uzol
Ortak Tez Yöneticisi: Yard. Doç. Dr. Nilay Sezer Uzol

Aralık 2009, 78 sayfa

Bu tezin kapsamı yeni geliştirilen aerodinamik analiz aracı AeroSIM+'ın kabiliyetlerini ortaya çıkarmak ve arka arkaya ileri uçuş yapan iki helikopterin rotor-rotor aerodinamik etkileşimlerini incelemektir. AeroSIM+ serbest iz bölgesi modellemesine dayanan, üç boyutlu, zamana bağlı panel metod potensiyel akış çözücüdür. Elde edilen sonuçlar askı durumundaki Caradonna-Tung rotorunun deneysel verileri ile doğrulanmıştır. AeroSIM+ ileri uçuş koşulu için geliştirilerek palaların rotor dinamiğine uygun şekilde hareketleri sağlanmıştır. Simulasyonlarda pala üzerindeki yüklerin girdap özü büyüklüğündeki değişikliklere duyarlı olduğu görülmüştür. Kanat-girdap etkileşim yerleri arkadaki rotorun lokasyonuna ve ileri uçuş hızına göre değişmektedir. Arkadaki rotorun performans karakteristiklerinin asimetrik akış bölgesindeki rotorların bağıl konumlarına göre değiştiği gözlemlenmiştir. Bu tez çalışmasının sonuçları, her rotor için hesaplanan kuvvet ve momentler ve bu yüklerin frekans karakteristikleri, helikopter dinamiği simülatörlerinde de kullanılabilir.

Anahtar Kelimeler: helikopter, serbest iz bölgesi, aerodinamik etkileşim

to my family

ACKNOWLEDGEMENTS

I would like to express my deepest gratitude to my supervisor, Asst. Prof. Dr. Oğuz Uzol for guidance, motivation and critical evaluation of my work. He helped me better understand the underlying physical principles and stay focused on the ultimate goal. Also I would like to thank my co-supervisor Asst. Prof. Dr. Nilay Sezer Uzol for her support and encouragement. They are the pioneers of this work who oriented me towards the right direction whenever necessary.

I would like to thank Prof. Dr. Cahit Çıray. He enlightened me on helicopters during my undergraduate years. I would like to express my sincere gratitude to Ilkay yavrucuk for his comments and suggestions about rotor dynamics. I would like to thank Onur Tarımcı for his friendship, useful discussions and support. Without the flight dynamics data provided by Onur, the analysis with trim conditions would have been impossible. I would like to thank my dear friends Pınar Şahin, Özlem Ceyhan, Belma Tavlar, Selvi Talipoğlu and Özge Demir for their encouragement and being on my side during the whole thesis study.

My parents and my brother have endured my absence with patience and understanding. They have never failed in believing in my capabilities to complete this challenging task. I will never have words to thank them enough.

Last but definitely not least, I would like to extend a heartfelt thanks to my dear beloved Alper. His endless love, understanding and encouragement had the biggest effect on my success. I could not have done it without him. Thank you, not only for your supporting me through this, but also for all the sunshine you have brought to my life.

TABLE OF CONTENTS

LIST OF FIGURES

FIGURES

LIST OF TABLES

TABLES

LIST OF SYMBOLS

q	Induced Velocity
Γ	Vortex strength
Rpm	Revolutions per minute
R	radius of the blade
c	Chord
γ	Lock number
C_T	Thrust coefficient
T	Thrust
ρ	Density
Ω	Angular velocity
rcore	Vortex core radius
C_P	Pressure coefficient
Ψ	Azimuth angle
θ	Blade pitch angle
θ_0	Collective pitch angle
θ_{1c}	Longitudinal swashplate angle
θ_{1s}	Lateral swashplate angle
β	Blade flapping angle
β_0	Coning angle
β_{1c}	Longitudinal flapping angle
β_{1s}	Lateral flapping angle
β_{shaft_tilt}	Shaft tilt angle
$\beta_{helicopter\_pitch}$	Helicopter pitch angle in body axis
$\beta_{helicopter\_roll}$	Helicopter roll angle in body axis
F_X	Resultant force in inertial frame x-axis
F_Y	Resultant force in inertial frame y-axis
F_Z	Resultant force in inertial frame z-axis
M_X	Resultant moment in inertial frame x-axis

M_Y Resultant moment in inertial frame y-axis

M_Z Resultant moment in inertial frame z-axis

CHAPTER 1

INTRODUCTION

Unlike a fixed wing aircraft, rotary wing aircraft generate lifting, propulsive and control forces all by a single component: the main rotor. In hover, the helicopter rotor provides lift in order to overcome the weight of the helicopter. The velocity distribution on the blades is linear with a zero velocity at the hub center and a maximum velocity at the tip of the blade. Each blade encounters the same velocity distribution throughout the azimuth. However, in forward flight, the helicopter rotor needs to provide a propulsive force in addition to the lifting force. The pilot uses cyclic controls to tilt the tip path plane forward so that the helicopter moves in that direction. In this case, thrust has two components, one opposing the weight and other compensating for the drag. Because of the freestream velocity, the velocity distribution varies as a function of the azimuth. The velocity reaches a maximum at the advancing side and a minimum at the retreating side. Due to this asymmetry, the aerodynamic loads on the blades alter as a function of the azimuth, which results in a periodic variation of the airloads.

1.1 Rotor Flow Field Characteristics

Helicopter rotor flow fields with their three-dimensional and unsteady nature are one of the most complex and hard-to-predict flows in aerodynamics. The vortical wake behind the rotating blades complicates the flow field. The wake of a helicopter rotor is dominated by concentrated vortices trailing at the blade tips as well as vorticity shed from the blade surfaces [1]. In hover, the tip vortices follow a helical trajectory as they are convected below the rotor disk area. The wake characteristics of a hovering single blade are shown in Figure 1.1. The induced velocity along the blade is highest at the blade tip. Therefore, the axial convection of the tip vortices is slower than the vortex

sheet along the blade [2]. The trailing tip vortex moves radially inboard of the blade which results in a radial contraction of the wake boundary [3].

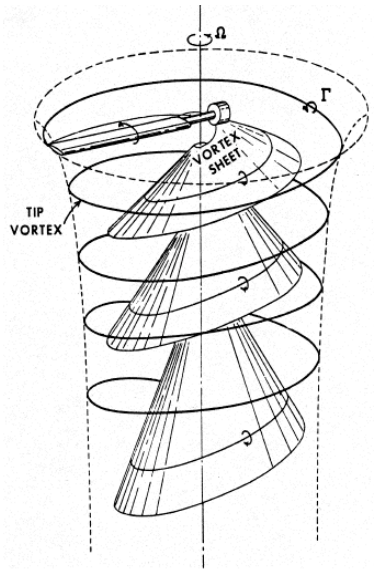

Figure 1.1 *Wake model of a hovering rotor (single blade) [3]*

As in hover, in forward flight the dominant feature in the wake is the tip vortices. In this case, the wake is also skewed back behind the rotor by the free stream velocity. This causes more distortion and more complicated form of the rotor wake. Figure 1.2 shows the representative views of the tip vortices in forward flight conditions. The wake structure of a rotor in forward flight is sensitive the free stream velocity and the orientation of the Tip Path Plane. An increase in the forward speed of the helicopter results in a higher the wake skew angle. Moreover, the tail rotor or the presence of a second main rotor (such as in tandem, coaxial and tilt rotor configurations) alters the induced velocity field, thus resulting in different wake geometry [2].

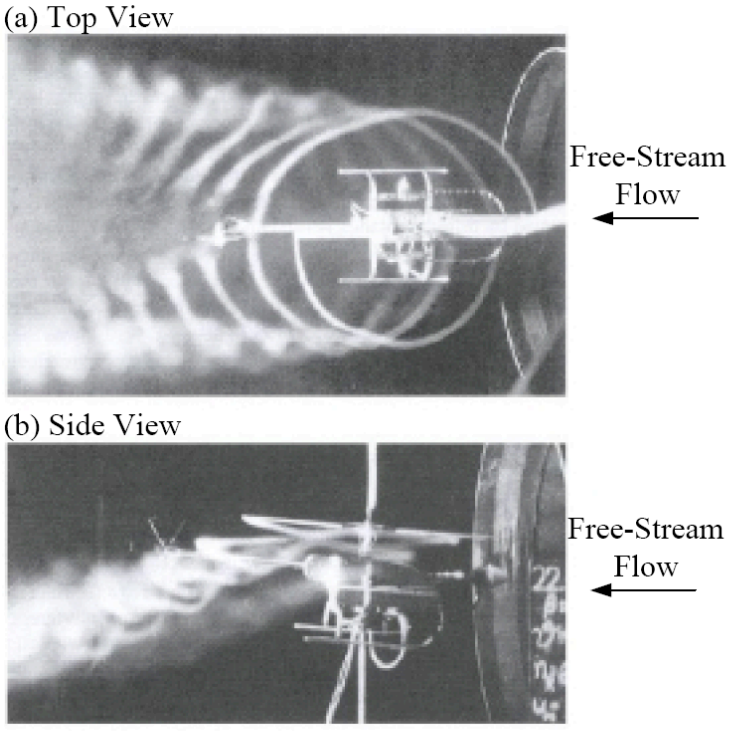

Figure 1.2 *Smoke visualization of the tip vortex locations in a two-bladed rotor wake in forward flight [2]*

Strong tip vortices appear both in fixed wing and rotary wing aircraft. For a fixed-wing aircraft, the tip vortices trail downstream so that the wake induced effects have little influence in the near field. In contrast, for helicopters, tip vortices remain close to the rotor disk area for many rotor revolutions and interact with individual vortex filaments, blades, other rotor systems and non-rotating components like the fuselage. These interactions add to the complexity of the flow field around helicopters and are illustrated in Figure 1.3. Accurate modeling of this complex flow plays a crucial role for determining the performance characteristics and predicting the loads on the rotor blades, and this is a challenging task for helicopter aerodynamics analyses.

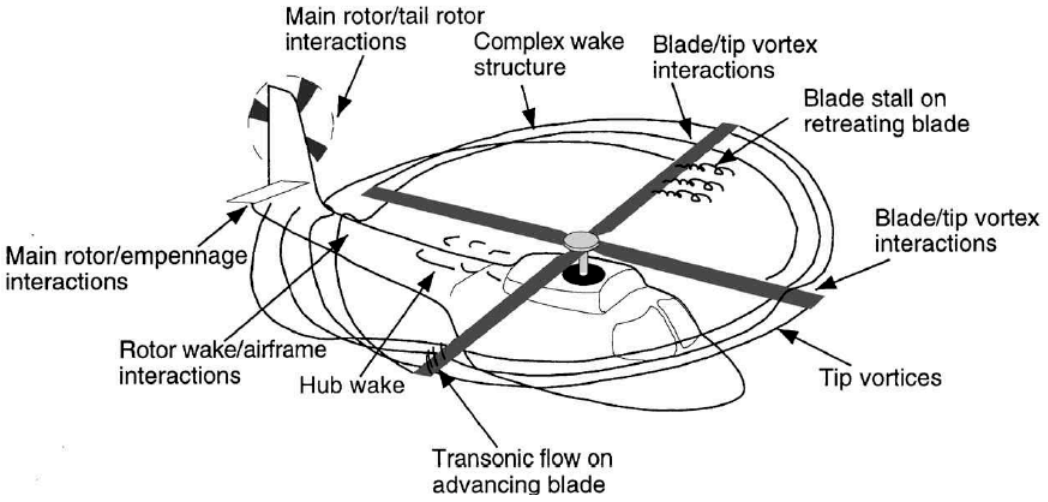

Figure 1.3 *Rotor wake and its interactions in forward flight [1]*

1.2 Interactional Aerodynamics in Rotorcraft

The main rotor wake interacts with other components of the helicopter, such as the airframe, tail rotor and empennage. Moreover, the presence of a second rotor (such as in tandem, coaxial and tilt rotor configurations) changes the induced velocity field. In addition to the interactions with other components, the dominant tip vortices interact with the blades. These interactions may cause undesirable effects on the performance, handling qualities and the acoustics. Therefore, in recent years, the interactional aerodynamic phenomena have received considerable attention. Types of interactions around the helicopter flow fields are summarized as follows:

1.2.1 Blade Vortex Interaction

The interaction of the strong tip vortices with the rotor blades is known as blade/vortex interaction (BVI) and is the major source of helicopter noise. The tip vortices remain close to the rotor and impinge on the blades. These interactions cause unsteady impulsive aerodynamic loads on the blades and blade vortex interaction (BVI) noise [4]. The intensity of the interactions depend on the local strength of the tip vortices, the viscous core radius of the vortex, the relative velocity of the tip vortex relative to the rotor blade, the miss distance between the tip vortex and the blade and the location of the BVI on the

rotor disk. The strongest BVI usually occurs at the advancing side because of the higher Mach numbers. McCroskey [5] and Yu [6] specified that the leading factors in the blade-vortex interactions are the strength of the vortex and the miss distance. Even small changes in miss distance can produce significant differences in the nature of the acoustic behavior.

The BVI problem is severe in low speed descending flight or maneuvering flight since it produces high blade loads and excessive noise [7]. Because of the annoyance for people in the surrounding area, rotorcraft noise reduction is vital for the development of the civil market of helicopters [8]. As for the military helicopters, the blade – vortex interaction noise is also important for the detection. Yu et al have investigated the active rotor control techniques for blade-vortex interaction noise reduction [9].

1.2.2 Rotor – Airframe Interaction

Besides the aerodynamic interactions of the blades with its own vortices generated by preceding blades, the main rotor wake also affects the airframe. The rotor wake encloses the significant parts of the airframe, especially in hover and low speed forward flight. In these flight conditions, the wake is convected almost downward and impinges on the airframe, as shown in Figure 1.4.

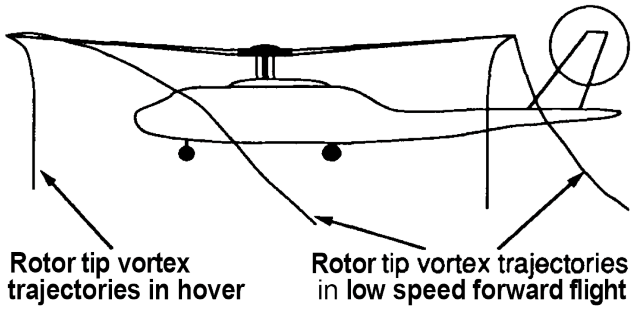

Figure 1.4 *Rotor Wake- Airframe Interactions in hover and forward flight [10]*

The rotor wake interaction with airframe is an extremely complex and unsteady process. It may cause relatively large forces and pitching moments. The impingement of the wake

on the fuselage may affect the performance and handling qualities [2, 11, 12]. The handling qualities are influenced by the impulsive loads that occur on the fuselage. These unsteady loads are induced by the pressure field due to the rotating blades. Moreover, the fuselage loads may be transmitted to the cabin in terms of vibrations and noise and thus may be annoying to passengers.

1.2.3 Main Rotor – Tail Rotor Interaction

The tail rotor is mounted on the tail boom of the helicopter, with a lateral axis of rotation. The thrust created by the tail rotor is offset from the center of gravity so that the tail rotor produces anti-torque balancing the torque of the main rotor. The pitch angles of the tail rotor blades are adjustable by the pilot via tail rotor pedals, which allows the pilot to control the yaw motion of the helicopter around its vertical axis. For a straight flight, the pitch of the tail rotor is set to prevent the helicopter from turning to the right since the main rotor turns to the left.

The tail rotor blades interact with the main rotor wake. The location of the tail rotor with respect to the main rotor and the gap between them affect the intensity of the aerodynamic interactions [13]. These interactions result in unsteadiness of the tail rotor performance which may cause strong negative influence on the dynamics of the helicopter. In addition, this interaction can be a significant source of tail rotor noise [14].

1.2.4 Main Rotor – Main Rotor Interaction

Multi rotor systems, such as coaxial, tandem, tilt rotor configurations, have mutual interference effects between the wakes generated by the rotors. The presence of the second rotor alters the induced velocity field. Therefore, different wake geometries are obtained. The proximity of the rotors and the amount of overlapping affect the intensity of the interactions.

Multi rotor systems can be classified as coaxial, tandem and tilt rotor configurations.In coaxial rotor helicopters, the rotors are turning in opposite directions in the same axis of

rotation, one above the other. There is an overlapping of the two rotors. The lower rotor partially operates in the wake of the upper rotor. Tandem rotor helicopters have two rotors mounted one in front of the other. The counter-rotating rotors are significantly overlapping and separated by a vertical gap. The rear rotor is set higher than the forward rotor. The rear and forward rotor wakes have a strong interaction especially in hover or low speed forward flight [15]. A tiltrotor aircraft has a lift capability with tiltable rotating propellers, or proprotors, used for both lift and propulsion. For vertical flight, the aircraft operates identical to a helicopter by tilting the proprotors to generate vertical thrust. As the aircraft accelerates, the proprotors are slowly tilted forward acting as a turboprop aircraft. The interactions between the wakes of proprotors may result in distorted wake structure which may affect the rotor airloads and the performance.

Figure 1.5 *Multi-Rotor Configurations. (a) Coaxial [16] (b) Tandem [17] (c) Tilt-rotor [18]*

1.3 Previous Research on Interactional Aerodynamics

In recent years, attention to interactional aerodynamic phenomena in helicopters has increased [11]. There have been both experimental and computational investigations that concern interactional problems.

First work on the rotor wake – fuselage interaction was done by Wilson and Mineck in 1975 [19]. They established that a smaller clearance between the main rotor and the fuselage can intensify the interactional effects in terms of higher induced airloads and vibration levels on the airframe. Wind tunnel experiments by Wilson and Mineck [19], Sheridan and Smith [20], Smith and Betzina [21], McMahon et al. [22], and Leishman & Bi [11] have shown that the rotor wake induces pressure loads on the fuselage.

Wilby et al. [23] and Betzina et al. [24] have shown the reciprocal effect that the airframe affects the loads and performance of the main rotor.

Pegg and Shidler carried out wind tunnel tests investigating the tail rotor noise due to interaction effects [14]. Fletcher and Brown have emphasized that the main rotor wake causes both unsteadiness and nonlinearity to the tail rotor performance [25].

The improvements in the large-scale computational techniques result in the possibility to simulate entire helicopter configurations. The streakline patterns for the V-22 Tiltrotor (operating in the helicopter mode) were simulated by Meakin [26] and shown in Figure 1.6.

Figure 1.6 *Wake Structure for V-22 Tilt Rotor [26]*

Akimov et al. [27] have emphasized the interacting wake structure of a coaxial Kamov Ka-32 helicopter with smoke injection near the tips of the rotor blades for different advance ratios. Bagai and Leishman [15] have used this experimental data to compare the wake prediction of their free-wake code. Brown [28] has used both results to verify his computational rotor wake model based on the numerical solution of the unsteady fluid-dynamic equations.

1.4 Objectives and Thesis Contents

The focus of the present study is to develop and examine the capabilities of a new aerodynamic analysis tool, AeroSIM+, and better understand the rotor–rotor aerodynamic interactions. AeroSIM+ is a 3-D unsteady vortex panel method potential flow solver based on a free vortex wake methodology. The methodology of the free vortex wake and the governing equations are explained in Chapter 2. The solver is validated using the experimental data from the Caradonna-Tung Experiments. The validation results are presented in Chapter 3. For the interactional analyses, two UH1H rotors are investigated in forward flight in which the rear rotor operates in the wake of the leading rotor. A series of analyses will be performed by changing the position of the rear rotor with respect to the leading rotor. Moreover, the effect of the forward speed is also considered. The results are presented and discussed in Chapter 4. Finally, the thesis is concluded in Chapter 5, presenting the conclusions from this study and the future work. In the near future, the results of UH-1H interactions are expected to be used in helicopter flight dynamics simulators.

CHAPTER 2

FREE VORTEX WAKE METHODOLOGY

In the current study, 3-D unsteady vortex panel method potential flow solver based on free vortex wake methodology was used which is commonly used for the aerodynamics and wake dynamics analysis of rotating wings [29]. Free vortex wake is composed of a large number of discrete vortex segments which move to the force free locations under the influence of the local velocity induced by the vortices on the blades and in the wake. The vortex elements are allowed to freely deform until they take up the positions consistent with the velocity field [30]. Free vortex wake methods are categorized into relaxation methods and time-marching methods [2]. The present free wake model is based on the time-marching method where the motion begins with an impulsive start of the rotor with no initial prescribed wake.

2.1 Wake and Surface Discretization

The suction and pressure surfaces of the blades as well as the tip and root surfaces are discretized using quadrilateral panel elements, and vortex ring elements are placed within each element. The leading edge of each vortex ring is placed on the ¼ chord of each panel, and the collocation point is placed at the ¾ chord of the panel element. The discretization of the blade can be seen in Figure 2.1. The aft segments of the vortex rings along the trailing edge lie in the wake before the rotation of the blades and those aft segments form the first segment of the wake vortices. As the blade advances during the first time step, it forms the second segment and the first row of wake vortices is generated. As the blade advances the second time step, it forms the third segment and the second row of wake vortices is created. The wake structure is formed with this procedure and grows with time. The presentation of this advancement is shown in Fig.2-2.

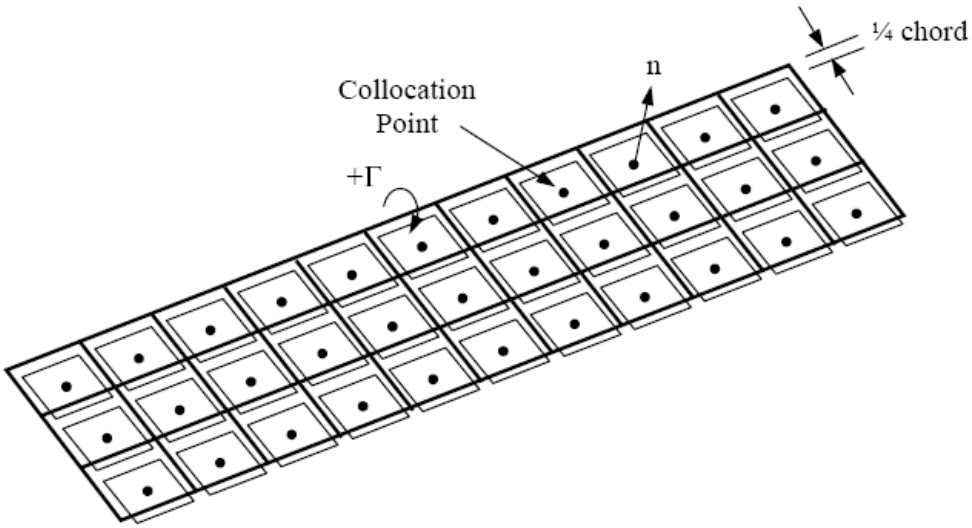

Figure 2.1 *Discretization of the blade [31]*

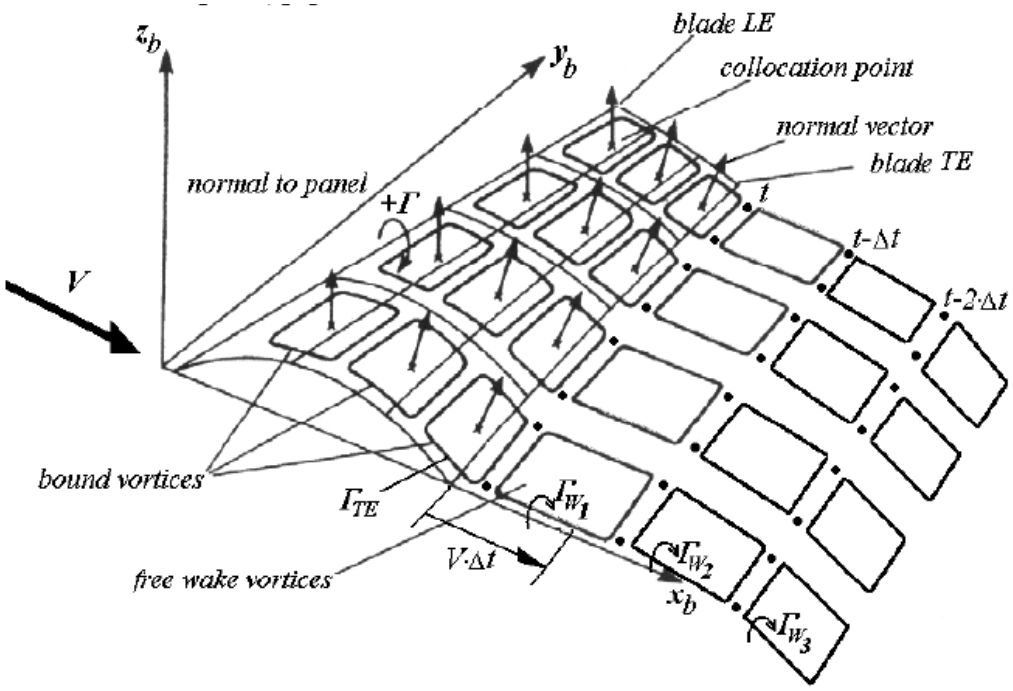

Figure 2.2 *Wake Shedding [30]*

2.2 Governing Equations

During an unsteady run, at each time instant the influence coefficients of surface panels are calculated using the induced velocity values from each vortex segment on the collocation points using Biot-Savart law. The unsteadiness comes from the unsteady motion of the boundaries. The derivation is as follows [32]

The continuity equation for incompressible flow is

$$\nabla \cdot \mathbf{q} = 0 \tag{2.1}$$

The velocity field can be expressed as the curl of a vector field **B,** such that

$$\mathbf{q} = \nabla \times \mathbf{B} \tag{2.2}$$

Since the curl of a vector is zero, **B** can be selected such that

$$\nabla \cdot \mathbf{B} = 0 \tag{2.3}$$

Thus the vorticity is

$$\zeta = \nabla \times \mathbf{q} = \nabla \times (\nabla \times \mathbf{B}) = \nabla(\nabla \cdot \mathbf{B}) - \nabla^2 \mathbf{B} \tag{2.4}$$

Applying equation (2.3), the vorticity equation reduces to Poisson's equation for the vector potential **B**

$$\zeta = -\nabla^2 \mathbf{B} \tag{2.5}$$

Using Green's Theorem, **B** is evaluated at point P at a distance r_0 from the origin due to the vorticity integration at point r_1 within the volume V, as shown in Fig. 2.3.

$$\mathbf{B} = \frac{1}{4\pi} \int_V \frac{\zeta}{|\mathbf{r}_0 - \mathbf{r}_1|} \, dV \tag{2.6}$$

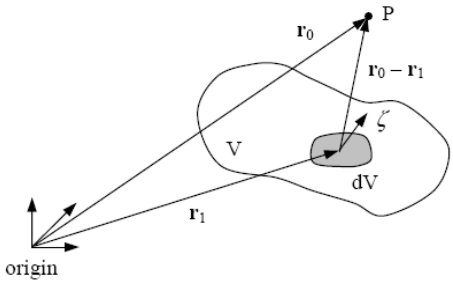

Figure 2.3 *Velocity at a point P due to a vortex distribution [32]*

Substituting this into equation (2.2), the velocity field at P is the curl of **B**

$$\mathbf{q} = \frac{1}{4\pi}\int_V \nabla \times \frac{\zeta}{|\mathbf{r}_0 - \mathbf{r}_1|}\, dV \tag{2.7}$$

Considering an infinitesimal vorticity filament ζ, shown in Fig. 2.4, where dS is normal to ζ, and the direction $d\mathbf{l}$ on the filament, the circulation Γ is

$$\Gamma = \zeta\, dS \tag{2.8}$$

$$dV = dS dl \tag{2.9}$$

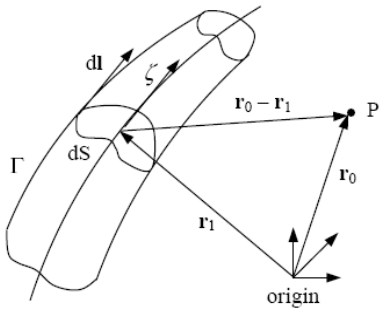

Figure 2.4 *Velocity at point P induced by a vortex segment [32]*

Substituting equations (2.8) and (2.9) into the integrand in equation (2.7) results in

$$\nabla \times \frac{\zeta}{|\mathbf{r}_0 - \mathbf{r}_1|} dV = \nabla \times \Gamma \frac{d\mathbf{l}}{|\mathbf{r}_0 - \mathbf{r}_1|} \tag{2.10}$$

Keeping $\mathbf{r}_1$ and d$\mathbf{l}$ fixed,

$$\nabla \times \Gamma \frac{d\mathbf{l}}{|\mathbf{r}_0 - \mathbf{r}_1|} = \Gamma \frac{d\mathbf{l} \times (\mathbf{r}_0 - \mathbf{r}_1)}{|\mathbf{r}_0 - \mathbf{r}_1|^3} \tag{2.11}$$

Substituting this result into equation (2.7) concludes the Biot-Savart Law:

$$\mathbf{q} = \frac{\Gamma}{4\pi} \int \frac{d\mathbf{l} \times (\mathbf{r}_0 - \mathbf{r}_1)}{|\mathbf{r}_0 - \mathbf{r}_1|^3} \tag{2.12}$$

Or in differential form

$$\Delta\mathbf{q} = \frac{\Gamma}{4\pi} \frac{d\mathbf{l} \times (\mathbf{r}_0 - \mathbf{r}_1)}{|\mathbf{r}_0 - \mathbf{r}_1|^3} \tag{2.13}$$

2.3 The Velocity Induced by a Straight Vortex Segment

The general form of the Biot-Savart Law is achieved considering the distance between the vortex segment and point P is **r**

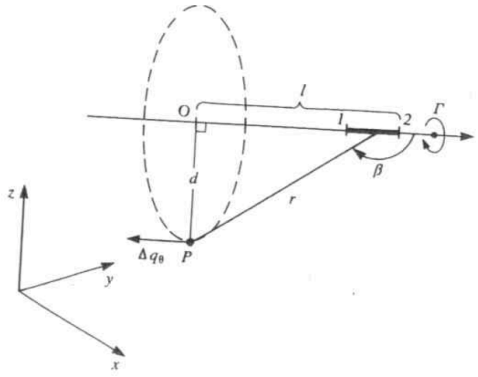

Figure 2.5 *Velocity Induced by a straight vortex segment [2]*

Therefore, equation (2.13) can be written in terms of the new notation:

$$\Delta\mathbf{q} = \frac{\Gamma}{4\pi}\frac{d\mathbf{l}\times\mathbf{r}}{r^3} \tag{2.14}$$

The cross product is

$$d\mathbf{l}\times\mathbf{r} = r\,dl\sin\theta \tag{2.15}$$

According to Fig.2.3

$$d = r\sin\beta \quad , \qquad \text{and} \quad r = \frac{d}{\sin\beta} \tag{2.16}$$

$$\tan(\pi-\beta) = \frac{d}{l} \quad , \qquad \text{and} \quad l = \frac{-d}{\tan\beta} \tag{2.17}$$

Differentiating equation (2.17) yields

$$dl = \frac{d}{\sin^2\beta}d\beta \tag{2.18}$$

Equation (2.14) can be rewritten in scalar form as

$$\Delta\mathbf{q} = \frac{\Gamma}{4\pi}\frac{d\mathbf{l}\times\mathbf{r}}{r^3} = \frac{\Gamma}{4\pi}\frac{r\,dl\sin\theta}{r^3} = \frac{\Gamma}{4\pi}(\sin\theta)\left(\frac{\sin^2\beta}{d^2}\right)\left(\frac{d}{\sin^2\beta}d\beta\right) \tag{2.19}$$

And therefore

$$\Delta\mathbf{q} = \frac{\Gamma}{4\pi d}\sin\beta\,d\beta \tag{2.20}$$

Equation (2.20) can be integrated over the length of the vortex segment

$$q = \frac{\Gamma}{4\pi d}\int_{\beta_1}^{\beta_2} \sin\beta \, d\beta = \frac{\Gamma}{4\pi d}\left(\cos\beta_1 - \cos\beta_2\right) \tag{2.21}$$

Thus, induced velocity depends on the strength Γ, distance d and the two angles β_1 and β_2.

For the two dimensional case in the case of an infinite vortex, where $\beta_1 = 0$ and $\beta_2 = \pi$ equation (2.21) becomes

$$q = \frac{\Gamma}{4\pi d}\int_{0}^{\pi} \sin\beta \, d\beta = \frac{\Gamma}{4\pi d}\left(\cos 0 - \cos\pi\right) = \frac{\Gamma}{2\pi d} \tag{2.22}$$

This result is consistent with the tangential velocity of a two-dimensional rigid cylinder.

For the general three-dimensional case equation (2.14) can be rewritten with geometric substitutions given below.

The vector connecting the edges of the vortex segment is $\mathbf{r}_0$

$$\mathbf{r}_0 = \mathbf{r}_1 - \mathbf{r}_2 \tag{2.23}$$

$$d = \frac{\left|\mathbf{r}_1 \times \mathbf{r}_2\right|}{\left|\mathbf{r_0}\right|} \tag{2.24}$$

$$\cos\beta_1 = \frac{\mathbf{r}_0 \cdot \mathbf{r}_1}{\left|\mathbf{r}_0\right|\left|\mathbf{r}_1\right|} \tag{2.25}$$

$$\cos\beta_2 = \frac{\mathbf{r}_0 \cdot \mathbf{r}_2}{\left|\mathbf{r}_0\right|\left|\mathbf{r}_2\right|} \tag{2.26}$$

The direction of the velocity $\mathbf{q}_{1,2}$ is

$$\frac{\mathbf{r}_1 \times \mathbf{r}_2}{\left|\mathbf{r}_1 \times \mathbf{r}_2\right|} \tag{2.27}$$

Above substitutions in equation (2.14) yields the final expression of an induced velocity of

$$\mathbf{q} = \frac{\Gamma}{4\pi} \frac{\mathbf{r}_1 \times \mathbf{r}_2}{|\mathbf{r}_1 \times \mathbf{r}_2|^2} \left[\frac{\mathbf{r}_0 \cdot \mathbf{r}_1}{r_1} - \frac{\mathbf{r}_0 \cdot \mathbf{r}_2}{r_2} \right] \tag{2.28}$$

2.4 Vortex Core Models

The flow is viscous inside the vortex core and viscous diffusion of the vortex filaments is included in free vortex wake models by incorporating a viscous core model. In current study, Rankine vortex model, which is the simplest model of a vortex with a finite core, is used. The core is modeled as a solid body rotation and the velocity inside the core is defined as

$$q_\theta(r) = \left(\frac{\Gamma}{2\pi r_c} \right) \left(\frac{r}{r_c} \right) \tag{2.29}$$

Inside the vortex core, the Biot-Savart Law is singular for $r \Rightarrow 0$. However, the tangential velocities should decrease in the core and tend to zero, as shown in Figure 2.6.

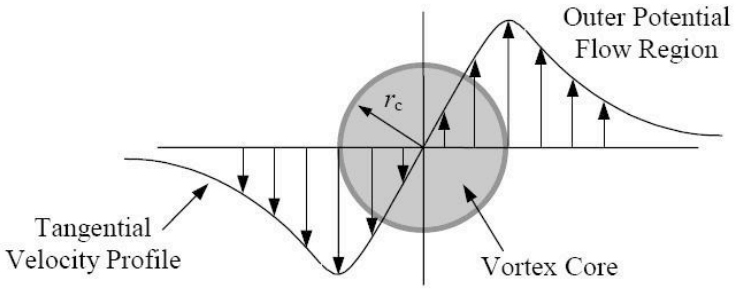

Figure 2.6 *Tangential velocity inside a tip vortex [2]*

An alternative vortex model is defined by Oseen and Lamb with a simplified form of the Navier Stokes equation [5].

$$q_\theta(r) = \left(\frac{\Gamma}{2\pi r_c \left(r/r_c \right)} \right) \left(1 - e^{-\alpha (r/r_c)^2} \right) \tag{2.30}$$

Where $\alpha = 1.25643$

Scully vortex model is commonly known in helicopter related studies [5].

$$q_\theta(r) = \left(\frac{\Gamma}{2\pi r_c} \right) \frac{r/r_c}{1 + \left(r/r_c \right)^2} \tag{2.31}$$

Another vortex model is given by Vatistas et al [5]

$$q_\theta(r) = \left(\frac{\Gamma}{2\pi r_c} \right) \frac{r/r_c}{\left[1 + \left(r/r_c \right)^{2n} \right]^{\frac{1}{n}}} \tag{2.32}$$

where n is an integer. For n=1, the tangential velocity reduces to the same equation used in Scully vortex model (equation (2.31)). For n $\rightarrow\infty$, it is the same as the Rankine vortex model. A comparison of these various vortex core models is shown in Figure 2.7

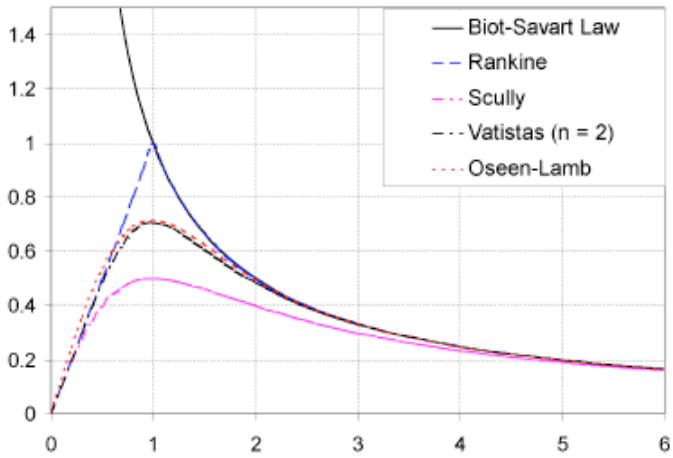

Figure 2.7 *Comparison of 2D vortex models [33]*

2.5 Determination of Lift

The induced velocity field can be computed by means of the Biot Savart Law once the position and the strength of the vortex filaments are known. The vortex strengths on the blades are solved for each time step with the implementation of zero normal flow across the solid surface boundary condition.

The normal velocity component on the surface on an arbitrary collocation point K is a combination of the self-induced velocity, wake- induced velocity and the free stream velocity. The strength of wake vortices is known from the previous time steps. Hence, the normal velocity induced by wake vortices can be calculated at each time step by using the Biot-Savart Law.
For an arbitrary collocation point K,

$$Q_{nK\_wake} = [u_W, v_W, w_W] \cdot \mathbf{n}_K \tag{2.33}$$

The normal velocity component due to free stream velocity is known from the kinematic equations.

$$Q_{nK\_\infty} = [U(t), V(t), W(t)]_K \cdot \mathbf{n}_K \tag{2.34}$$

The only unknown quantity is the velocity induced by the blade vortices. At each collocation point, the induced velocities are calculated using the Biot Savart Law. The Biot-Savart Law is rewritten as

$$\mathbf{q} = \left(\frac{1}{4\pi} \frac{\mathbf{r}_1 \times \mathbf{r}_2}{|\mathbf{r}_1 \times \mathbf{r}_2|^2} \left[\frac{\mathbf{r}_0 \cdot \mathbf{r}_1}{r_1} - \frac{\mathbf{r}_0 \cdot \mathbf{r}_2}{r_2} \right] \right) (\Gamma) \tag{2.35}$$

Transferring the known quantities to the right hand side gives up

$$RHS_K = -[U(t) + u_W, V(t) + v_W, W(t) + w_W]_K \cdot \mathbf{n}_K \tag{2.36}$$

When the boundary condition is applied to each of the collocation points, the following set of algebraic equations are obtained

$$\begin{pmatrix} a_{11} & a_{12} & a_{13} & \dots & a_{1m} \\ a_{21} & a_{22} & a_{23} & \dots & a_{2m} \\ a_{31} & a_{32} & a_{33} & \dots & a_{3m} \\ \vdots & \vdots & \vdots & \ddots & \vdots \\ a_{m1} & a_{m2} & a_{m3} & \dots & a_{mm} \end{pmatrix} \begin{pmatrix} \Gamma_1 \\ \Gamma_2 \\ \Gamma_3 \\ \vdots \\ \Gamma_m \end{pmatrix} = \begin{pmatrix} RHS_1 \\ RHS_2 \\ RHS_3 \\ \vdots \\ RHS_m \end{pmatrix} \tag{2.37}$$

Once the vortex strengths of each vortex ring are obtained, the blades are moved according to their respective kinematic motion to the next time step.

The force and moment components generated by the blades are performed by first obtaining the pressure coefficient variations on blade surfaces. The local pressure value is used to obtain local force and moment components acting on an individual panel. These forces and moments are added together to obtain the total force and moment of the rotor.

CHAPTER 3

CARADONNA-TUNG ROTOR SIMULATIONS

In the literature, many computational schemes used in helicopter rotor aerodynamics studies are checked against the extensive data set obtained from the experiments of Caradonna and Tung [34]. Therefore, a validation study is performed for the AeroSIM+ code using that dataset and the results are presented in this chapter.

3.1 The Caradonna - Tung Rotor

The Caradonna-Tung rotor has two blades with no twist, no taper, 1.143 m radius and an aspect ratio of 6 with a NACA 0012 airfoil section operating in hover. The collective pitch angle is set to 8^0 and the rotational speed is set to 1250 rev/min, which results in a 0.44 Mach number at the blade tips. The experimental set up is shown in Figure 3.1 [34].

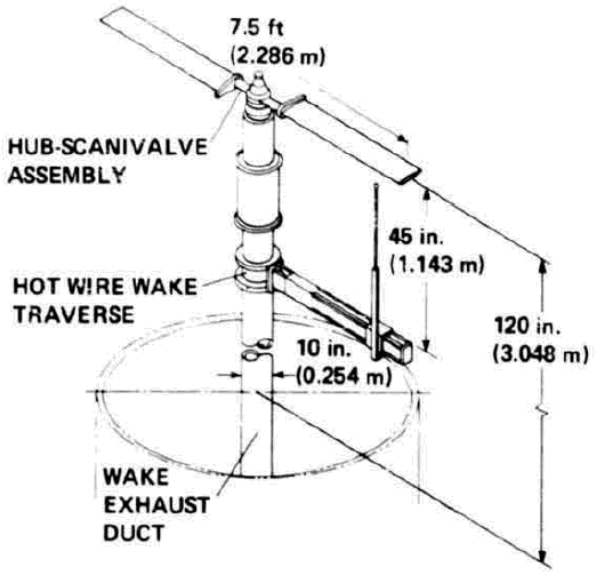

Figure 3.1 *Experimental set up of Caradonna-Tung Rotor [34]*

In the computations using the AeroSIM+, the blade rotation is impulsively started and the time increment is chosen such that the rotor blades advance 6°, at each time step. Therefore one revolution is completed in 60 time steps. The azimuthal discretization of one rotor revolution is illustrated in Figure 3.2. The computations are performed for 30 rotor revolutions. The rotor blade surfaces are discretized by 40 chordwise and 10 spanwise panels. The discretization of the blade surfaces is shown in Figure 3.3. Spanwise grid spacing is such that smaller panels are placed at the root and tip regions of the blade. Likewise, smaller panels are placed near the leading edge and trailing edges.

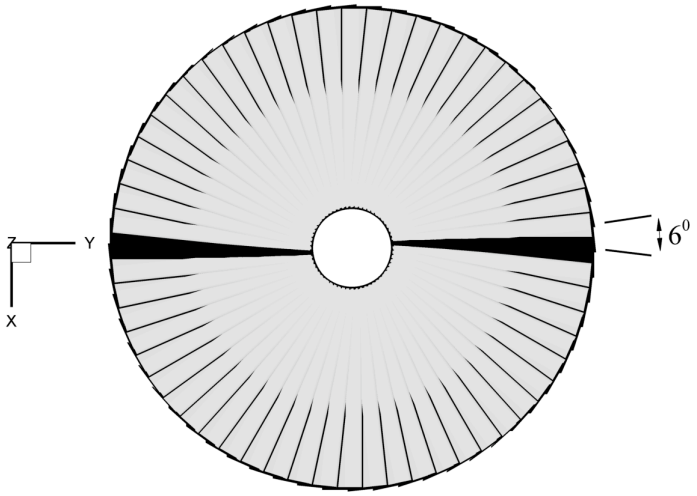

Figure 3.2 *Azimuthal discretization of one rotor revolution*

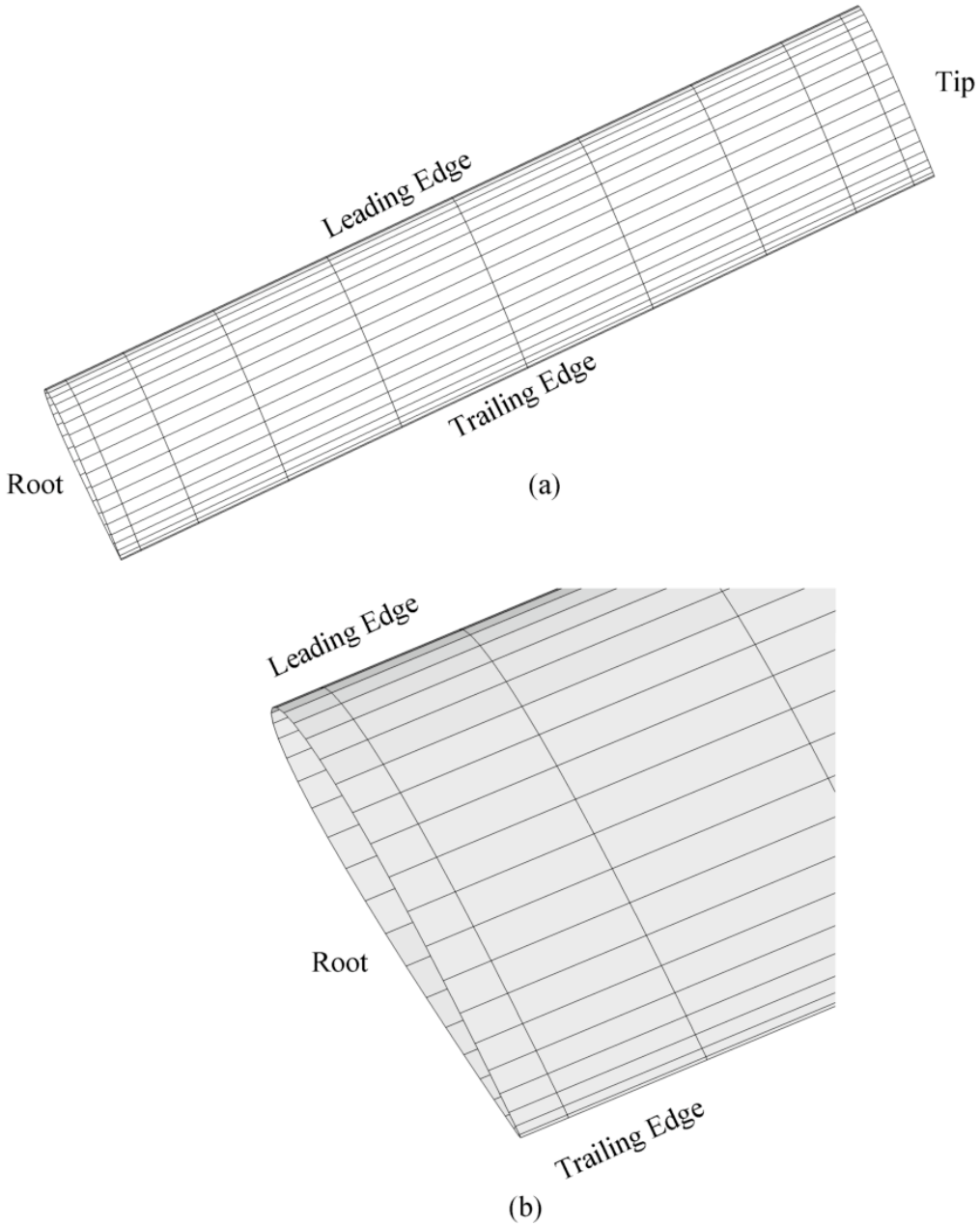

Figure 3.3 *Experimental Surface grid on a Caradonna-Tung rotor blade: (a) Spanwise grid spacing, (b) Chordwise grid spacing*

Figure 3.4 shows three different views of the structure of the wake below the rotor after 30 revolutions. As the blades rotate, the wake convects downstream with the local fluid velocity. The roll-up and trajectory of the tip vortices as well as the contraction of the wake are clearly visible in this figure.

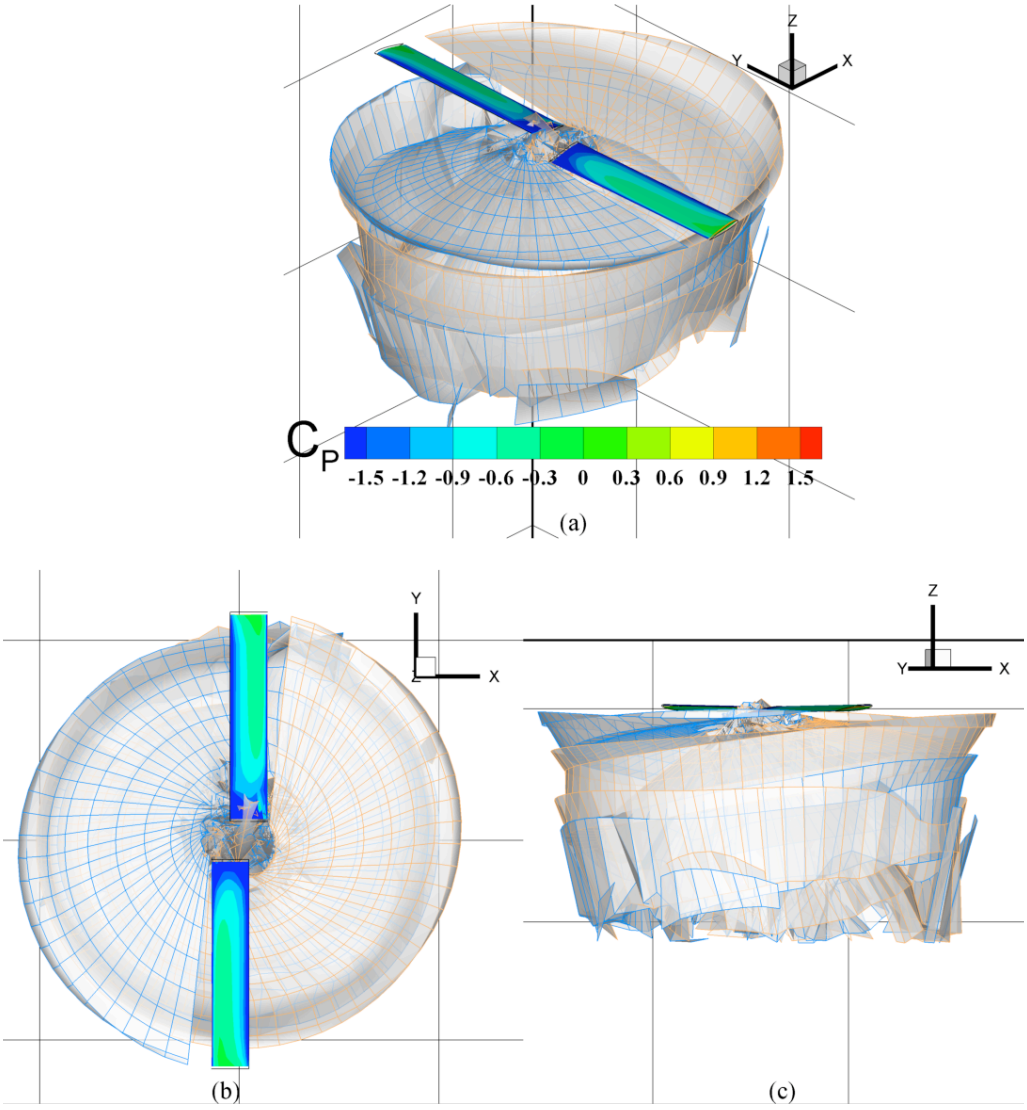

Figure 3.4 *Wake structure behind the Caradonna-Tung rotor: (a) Isometric view, (b) Top view, (c) Side view*

For a better understanding of the physical representation of a hovering Caradonna-Tung rotor, the calculated vortex strengths in each wake panel as well as the ones on blade surfaces are used to obtain the induced velocity field in a volume grid shown in Figure

3.5. The volume grid extends one diameter above and two diameters below the rotor disk to visualize the inflow through the rotor disk area and the high vorticity regions below the disk. For this purpose, the u,v,w velocities at each grid point is then used for the calculation of vorticitity components in three directions and the vorticity magnitude. Using the volume grid with the velocity and vorticity data, it is possible to visualize iso-vorticity surfaces showing root and tip vortices, location of the tip vorticies, volume streamlines and surface streamlines on any desired plane.

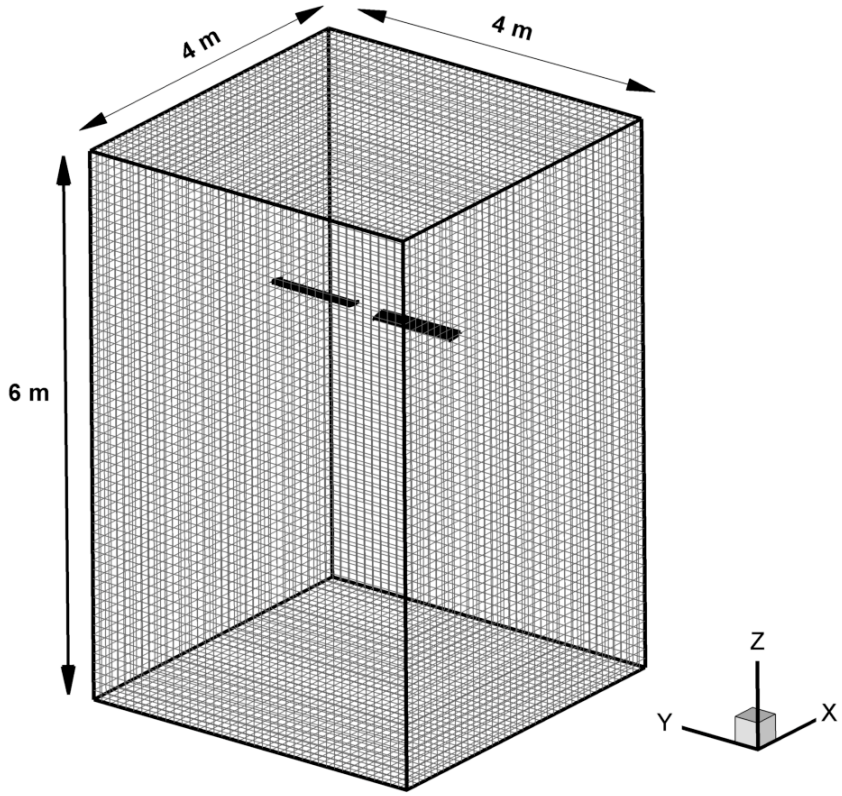

Figure 3.5 *Volume grid enclosing the rotor and the near wake behind the Caradonna-Tung rotor*

Figure 3.6 shows the velocity and vorticity distributions after 30 revolutions. The wake boundary and the contraction of the wake are clearly seen in Figure 3.6 (a). The flow velocity outside the wake boundary is zero as shown in the figures (a) and (b). The high vorticity region is seen at the blade root and tips and it is shown in Figure 3.6 (c). The tip

vortices occur behind the blades and trail below the blades following the helical trajectory.

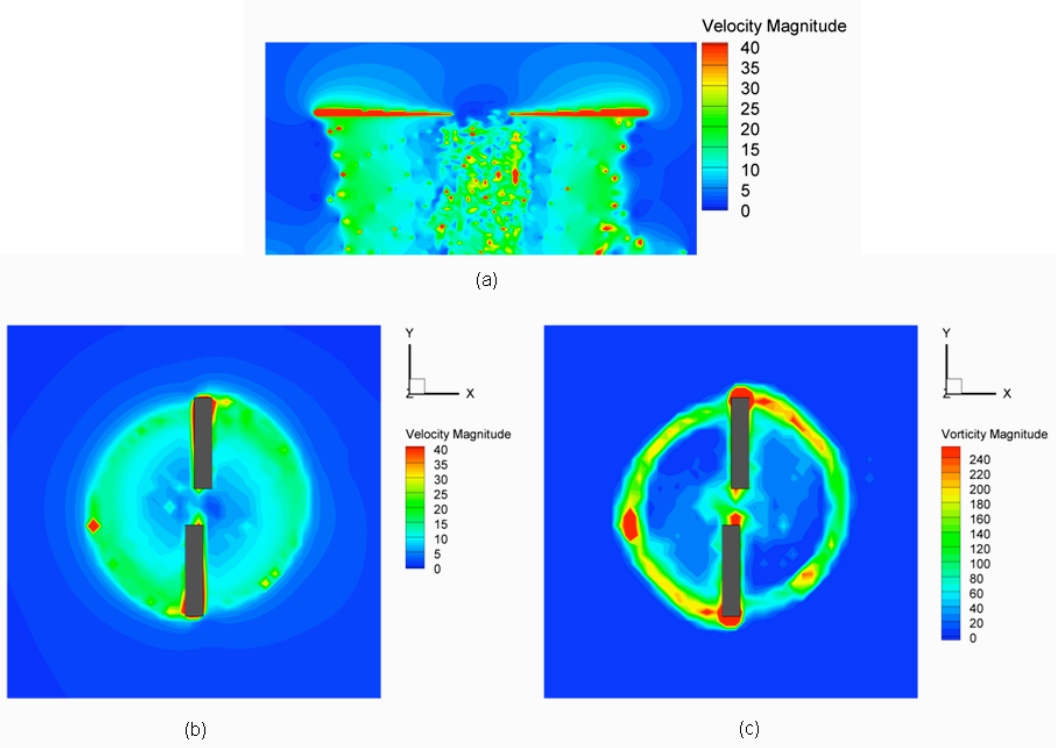

Figure 3.6 *Velocity and vorticity magnitude distributions within the wake of Caradonna-Tung rotor: (a) Velocity magnitude distributions within the wake on x=0 plane, (b) Velocity magnitude distributions within the wake on z=-0.03 plane, (c) Vorticity magnitude distributions within the wake on z=-0.03 plane*

The flow is viscous inside the vortex cores. Therefore, vortex core models should be used to define the velocity profile inside the vortices. Otherwise, by using the Biot-Savart Law, the velocity increases towards infinity at the vortex center. In AeroSIM+ code, it is possible to use different vortex core models that are explained in Chapter 2.

Figure 3.7 shows the variations of the computed thrust coefficient and the comparisons with the measured data in the experiments. The unsteady aerodynamic loads occur in the first 10 revolutions and then a steady-state solution is obtained. This is because of the fact that the blades are impulsively started and the wake of a hovering rotor is close to

the rotor disk for many revolutions. Wake convects below the rotor when the vortices start to retreat from the blades.

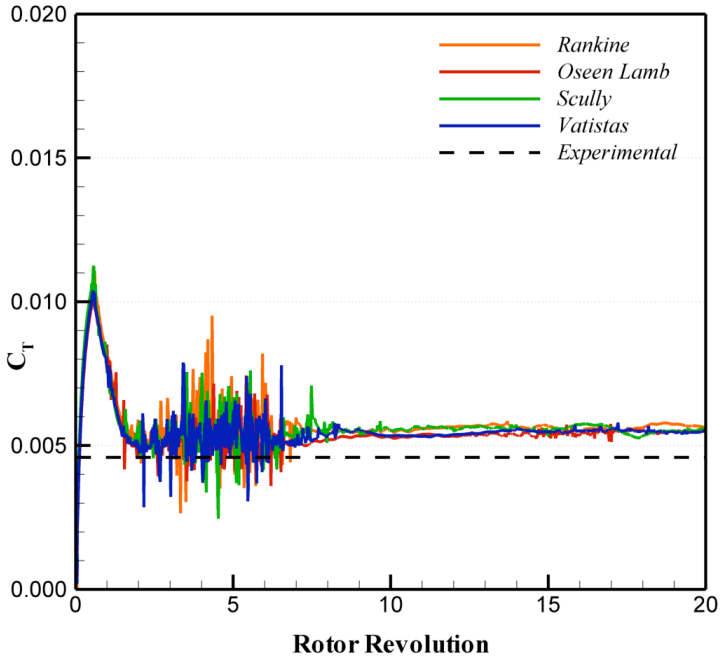

Figure 3.7 *The Total Thrust Coefficient (C_T) variations of Caradonna-Tung rotor at hover for different viscous core models using 0.001 m vortex core radius*

The total thrust coefficient is calculated as

$$C_T = \frac{T}{\rho \cdot (\pi R^2) \cdot (\Omega R)^2} \tag{3.1}$$

The effect of the viscous core model is investigated and presented in Figure 3.7. The vortex core radius used in these computations is 0.001 m. As it can be seen in the figure, AeroSIM+ results are not very sensitive to the viscous core model.

After the computations using different type of vortex models, the effect of core radius is investigated. As can be seen in Figure 3.8, the vortex core radius has a dominant effect on the computed value of the thrust coefficient since it changes the induced velocity field of the system. Selection of an appropriate core radius can produce results that are in very close agreement with the experiments. In Figure 3.8, the case with a vortex core radius of

0.0015 m (5.85% of the spanwise dimension of the smallest panel and 0.79% of the chord length) seems to be producing the best result.

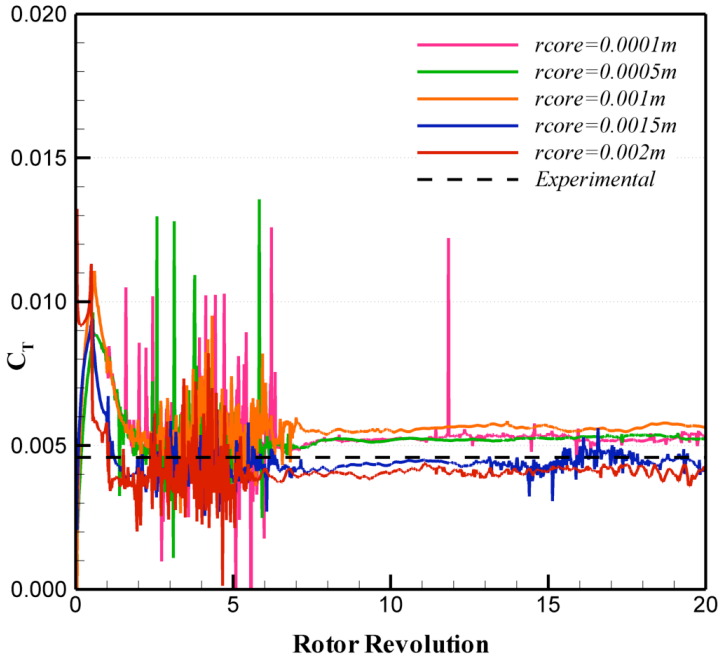

Figure 3.8 *The Total Thrust Coefficient (CT) variations of Caradonna-Tung rotor at hover for different viscous core radii using the Rankine vortex core model*

The surface pressure distributions of the case with a vortex core radius of 0.0015 m are compared with the experimental C_P distributions on the blades. The C_P comparisons at five different radius stations are shown in Figure 3.9. There's reasonable agreement between the experiments and computations. In addition to the chordwise C_P comparison, spanwise distribution is also compared with the experimental data Figure 3.10 shows the spanwise C_P distribution at the quarter chord. The distribution shows aggreement with the experimental data. However, the grid resolution needs to be improved.

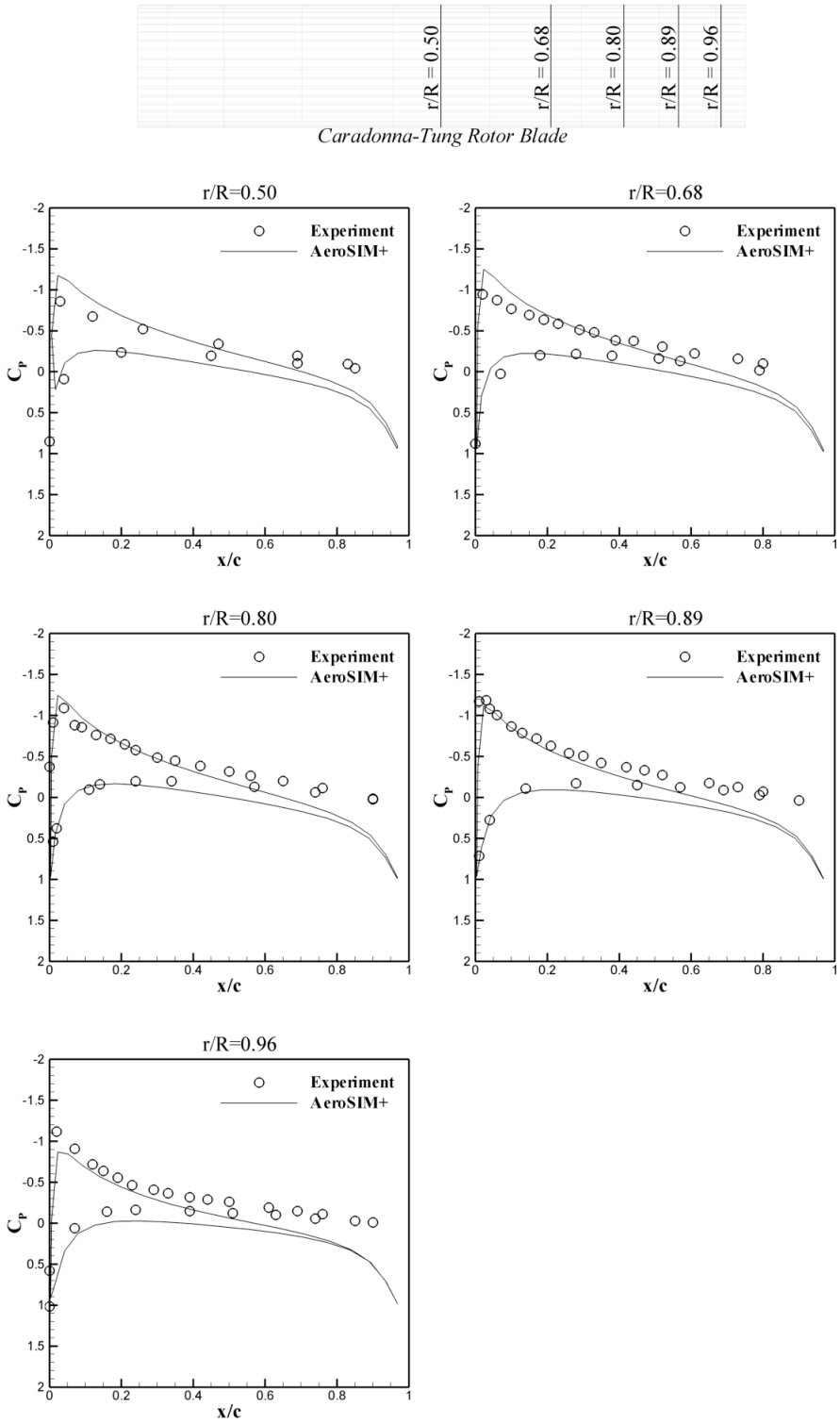

Figure 3.9 *Comparison of calculated chordwise CP distributions with experimental data at 50%, 68%, 80%, 89% and 96% span locations for the Caradonna-Tung rotor test case.*

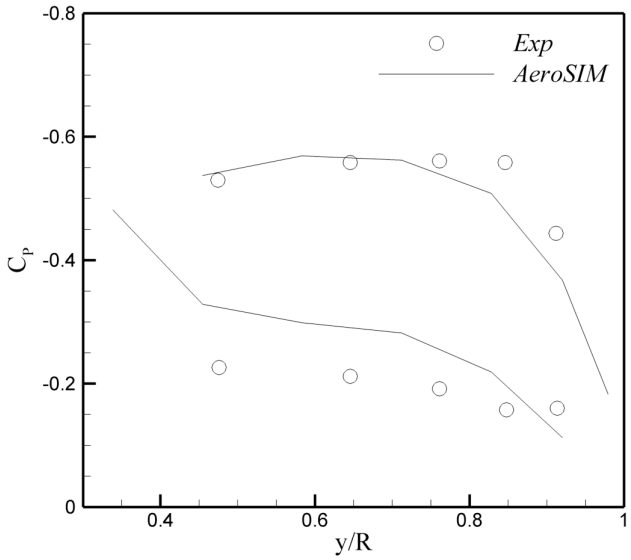

Figure 3.10 *Comparison of calculated spanwise CP distributions with experimental data at quarter chord line.*

CHAPTER 4

ROTOR – ROTOR INTERACTION SIMULATIONS IN FORWARD FLIGHT

The particular focus of the current study is to investigate the wake interactions between two UH-1H rotors operating in forward flight, one operating within the wake of the other. The interactions alter the induced velocity field of the system, resulting in the unsteadiness of the aerodynamic loading. Therefore, the rear rotor no longer generates the same amount of thrust. The interactions are severe when the rear rotor operates in close proximity to the front rotor. Therefore, the amount of reduction in thrust depends on the relative position of the rear rotor. Since the wake flow field of the front rotor is different on advancing and retreating sides, the interactional effects are different when the rear rotor is operating on starboard or port sides.

4.1 Rotor Geometry and Simulation Details

UH-1H rotor blades have NACA 0012 airfoil section, with a 0.5334 m chord length and 10.89 degree linear twist. The radius of the rotor disk is 7.3152 m and the rotational speed is 324 rev/min. The geometric information of UH-1H rotor is given in Table 4.1. The blade rotation is impulsively started and the time increment is chosen such that the rotor blades advance 6° at each time step, similar to the previous studies of Szymendera [31], Katz and Maskew [35]. Therefore, one revolution is completed in 60 time steps as can be seen in Figure 4.1. The rotor blade surfaces are discretized by 40 chordwise and 14 spanwise panels. The discretization of the blade surfaces is shown in Figure 4.2. In chordwise spacing, smaller panels are used near the trailing edge and leading edge of the blade. Similarly, in spanwise spacing, smaller panels are used near the root and tip of the blade.

Table 4.1 *UH1H Rotor Information*

Airfoil	*NACA0012*
Chord Length	0.5334 m
Radius	7.3152 m
Twist (linear)	-10.89 deg
Angular Velocity	324 rpm
Shaft tilt angle	5 deg

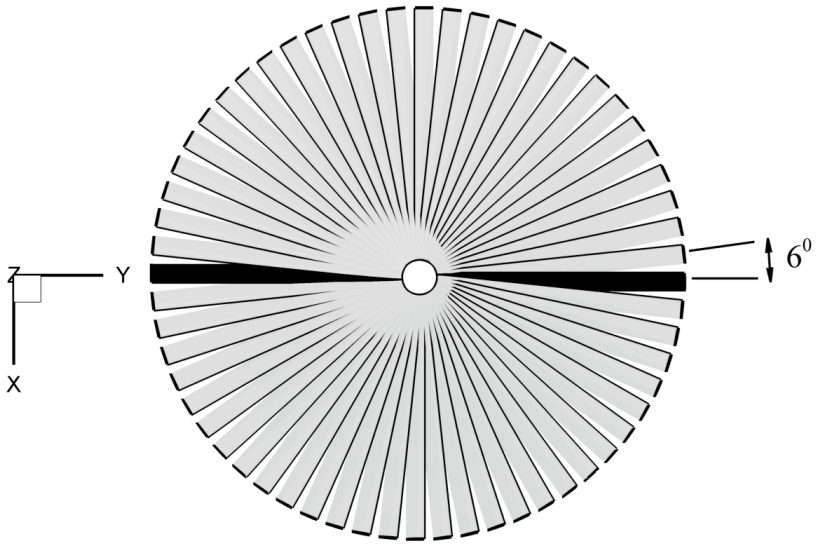

Figure 4.1 *Azimuthal discretization of one revolution*

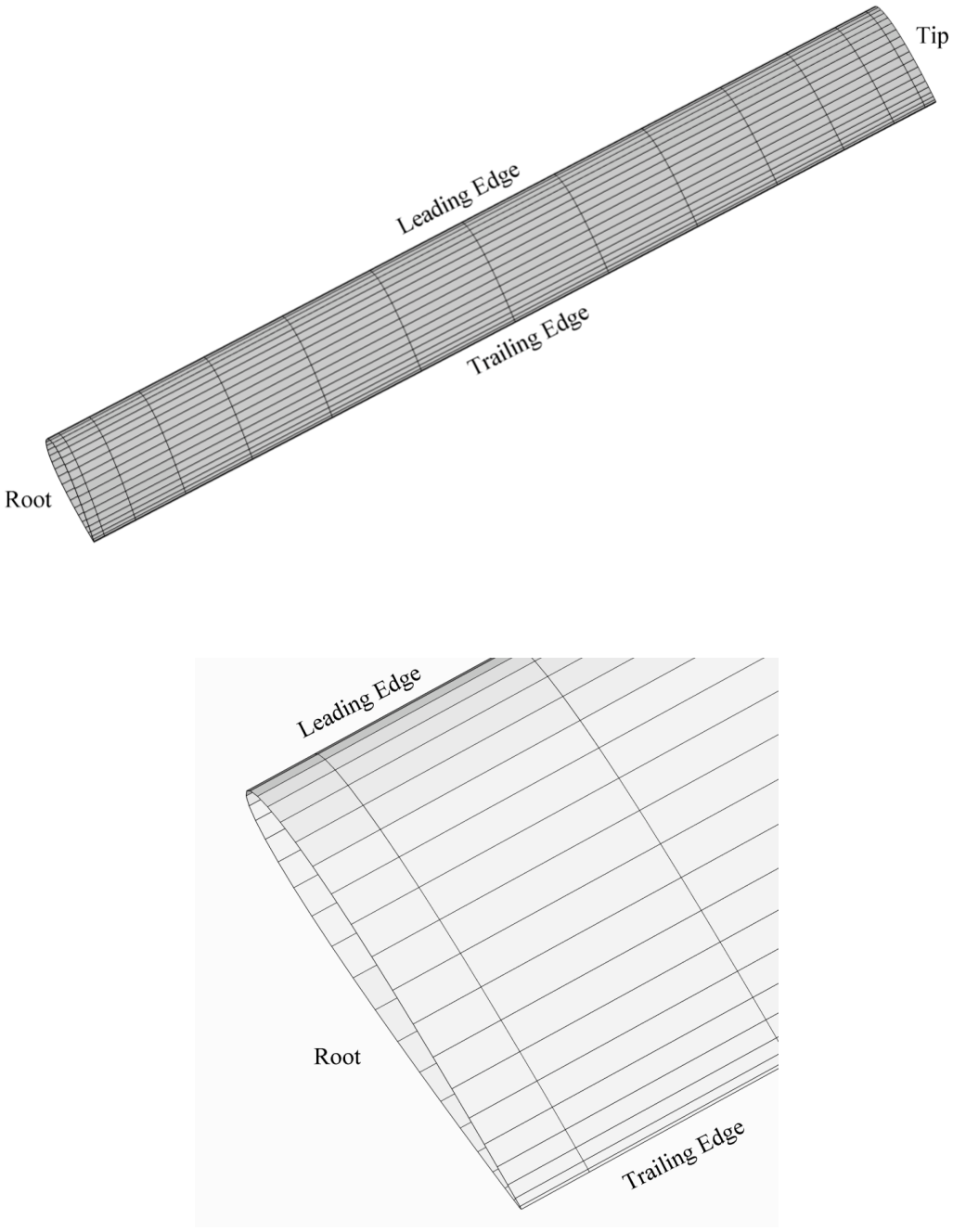

Figure 4.2 *Surface Grid on a UH-1H rotor blade: (a) Spanwise grid spacing, (b) Chordwise grid spacing*

4.2 Forward Flight Rotor Dynamics

In forward flight, the blades encounter asymmetric velocity field due to the freestream velocity. The maximum velocity is seen on the advancing side, and reaches a minimum on the retreating side. Due to the asymmetry of the flow, the aerodynamic forces are different in each azimuth position. The blades freely flap up and down due to the effect of these varying loads. Therefore, a trimmed rotor solution is essential for forward flight simulations.

AeroSIM+ code is developed for pitching and flapping motions of the blades in each time step. The azimuthal variation of the blade pitch angles during forward flight can be calculated using,

$$\theta(\psi) = \theta_0 + \theta_{1c} Cos(\psi) + \theta_{1s} Sin(\psi) \tag{4.1}$$

Collective pitch angle (θ_0), longitudinal swashplate angle (θ_{1c}) and the lateral swashplate angle (θ_{1s}) are the outputs of the flight control system and used directly in equation 4.1 to obtain the pitch angle of the blades in each time step. The trim values at different forward flight speeds are obtained using the flight control system developed by Tarımcı [36] and are presented in Table 4.2.

Table 4.2 Trim Values for Pitching Motion obtained using the flight control system developed by Tarımcı [36]

	θ_0 *[rad]*	θ_{1c} *[rad]*	θ_{1s} *[rad]*
Hover	0.258062	-0.049136	0.000144
60 knots	0.231658	-0.038162	0.001044
80 knots	0.249095	-0.048859	0.042587
100 knots	0.282299	-0.068243	0.105771

The azimuthal variation of the blade flapping angles during forward flight can be calculated using,

$$\beta(\psi) = \beta_0 + \beta_{1c} Cos(\psi) + \beta_{1s} Sin(\psi) \tag{4.2}$$

Coning angle (β_0), longitudinal flapping angle (β_{1c}) and lateral flapping angle (β_{1s}) are obtained using the flight control system as explained before. In order to define the orientation of the blades at each time step, the effects of shaft tilt angle, helicopter pitch angle and helicopter roll angle for a specified forward speed should also be considered because the current study covers only rotor simulations without the fuselage. For this purpose, the effect of shaft tilt and helicopter pitch are included in longitudinal motion of the blades and the helicopter roll angle is included in lateral motion of the blades.

The shaft tilt angle of the UH-1H rotor is 5 degrees. The shaft tilt changes the orientation of the Tip Path plane. Therefore, the azimuthal variation of the blade angles due to shaft tilt can be calculated using,

$$\zeta_{shaf\,t\_\,tilt}(\psi) = \zeta_{\,shaf\,t\_\,tilt} Cos(\psi) \tag{4.3}$$

The helicopter pitch angle is different for different forward speeds. The helicopter pitch angle changes the orientation of the Tip Path plane. Therefore, the azimuthal variation of the blade angles due to helicopter pitch can be calculated using,

$$\zeta_{helicopter\_\,pitch}(\psi) = \zeta_{helicopter\_\,pitch} Cos(\psi) \tag{4.4}$$

The helicopter roll angle is different for different forward speeds. The helicopter roll angle changes the orientation of the Tip Path plane resulting in a lateral tilt. Therefore, the azimuthal variation of the blade angles due to helicopter roll can be calculated using,

$$\zeta_{helicopter\_\,roll}(\psi) = \zeta_{helicopter\_\,roll} Sin(\psi) \tag{4.5}$$

The azimuthal variation of the blade angles are implemented to the AeroSIM+ code with the modified version of equation 4.2 such that

$$\zeta(\psi) = \beta_0 + \left[\beta_{1c} + \zeta_{shaft\_tilt} + \zeta_{helicopter\_pitch}\right] Cos(\psi) + \left[\beta_{1s} + \zeta_{helicopter\_roll}\right] Sin(\psi) \tag{4.6}$$

Coning angle (β_0) for hover is defined in Johnson [37] as

$$\beta_0 = \frac{\theta_0 \cdot \gamma}{8} \tag{4.7}$$

where, γ is the Lock Number which is defined in Johnson [37] as

$$\gamma = \frac{\rho \cdot C_{l\alpha} \cdot c \cdot R^4}{I_b} \tag{4.8}$$

where,

ρ=1.225 kg/m^3

$C_{l\alpha}$=6.3 rad^{-1}

c=0.5334 m

R=7.3152 m

I_b=1873.74 kgm^2

Using above values γ is found to be 6.2914.

In the current study, for forward flight simulations, coning angle is calculated using Equation 4.7.

Table 4.3 *Trim Values for Flapping Motion obtained using the flight control system developed by Tarımcı [36]*

	β_{1c} *[rad]*	β_{1s} *[rad]*	*Helicopter pitch angle [rad]*	*Shaft Tilt Angle [rad]*	*Helicopter roll angle [rad]*
Hover	-0.000144	-0.049136	0.089446	-0.087266	0.000571
60 knots	0.027263	-0.038461	-0.025764	-0.087266	0.002262
80 knots	-0.004977	-0.049355	-0.059052	-0.087266	0.002947
100 knots	-0.058955	-0.068760	-0.086977	-0.087266	0.004147

Figure 4.3 shows the result of longitudinal flapping of the UH-1H rotor blades. As the forward speed of the helicopter increases, the longitudinal tilt of the Tip Path Plane increases appropriately as expected.

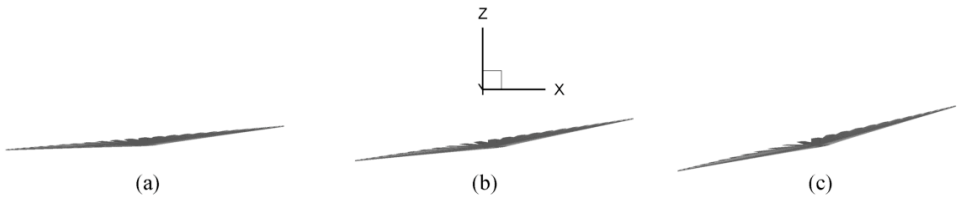

Figure 4.3 *Tip Path Plane of UH-1H rotor at different forward flight speeds: (a) 60 knots (b) 80 knots (c) 100 knots*

4.3 UH-1H SINGLE ROTOR SIMULATIONS

Before performing the interaction analyses of two UH-1H rotors, a single UH-1H rotor was simulated at hover and forward flight conditions. Single rotor simulations require less computational effort. The code was run 16 hours (wall clock) for obtaining 10 revolutions of a single rotor simulation. The simulations were performed on a machine which has Xeon Processor 3.00 Ghz / 1333 MHz with 2GB RAM. Therefore, the input variables are preferably tested in single rotor simulations. A proper core radius selection affects the aerodynamic loading as can be seen from the Caradonna-Tung simulations. Moreover, single rotor simulations are constructed in order to compare the results with the interaction simulation results. It is also possible to check the vertical force component with the weight of the UH-1H rotor.

Figure 4.4 shows the wake structure behind the UH-1H rotor at 60 knots forward flight condition. The wake is shed from the trailing edge of the rotor blades as it moves below the rotor disk area and convects downstream with the local fluid velocity. The roll up of the tip vortices is also evident in the figure. Figure 4.5 shows the top view of the tip vortices at 60 knots and 80 knots forward flight condition. The roll up of the tip vortices is also seen in this figure. The mutual interaction between the individual vortex filaments

causes distortion in the wake boundary. This distortion is strong for the 60 knots simulation because at low advance ratios the tip vortices are closest together for many revolutions.

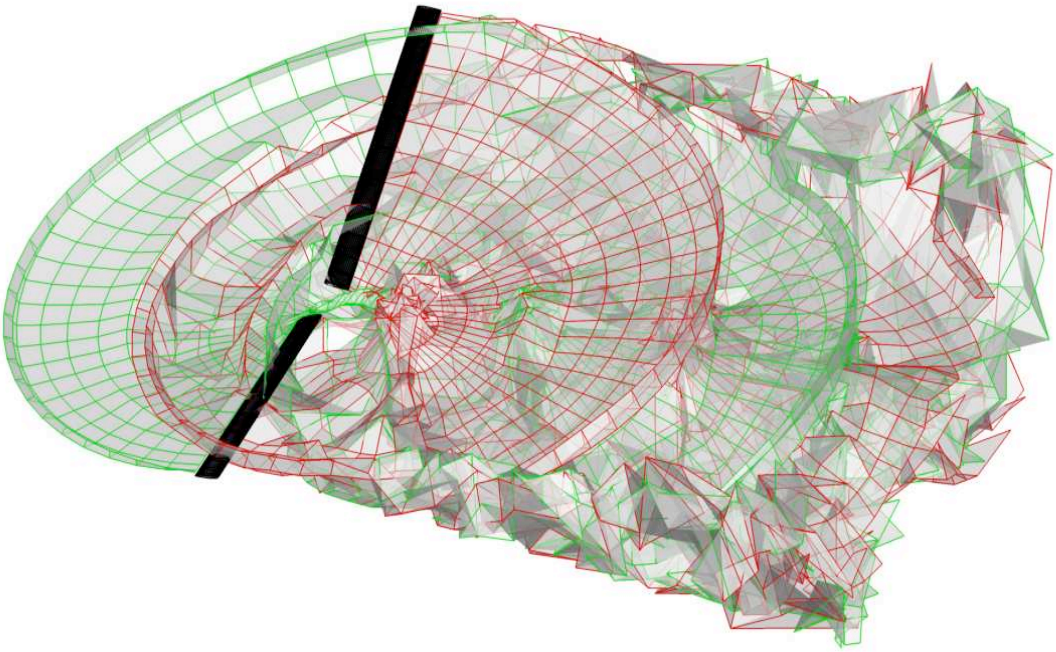

Figure 4.4 *Near wake structure behind the UH-1H rotor*

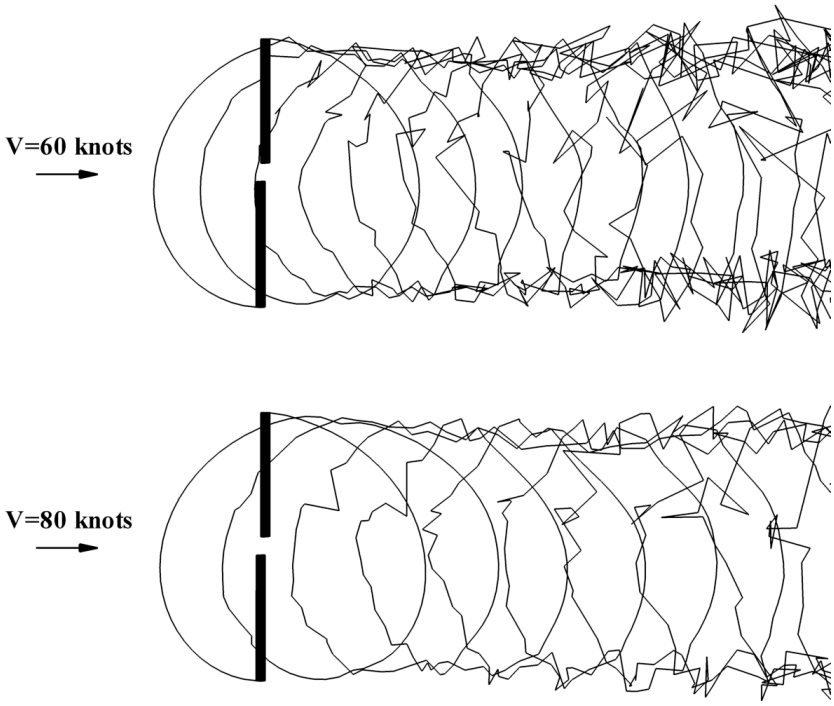

Figure 4.5 *Tip vortices from UH-1H rotor blades at 60 knots and 80 knots forward flight*

Wake flow and vortex structures can be better visualized by obtaining the induced velocity field in a volume grid. The induced velocities are calculated by using the circulation distributions at each wake panel. The volume used to visualize UH-1H single and multi rotor simulations extends up to 4 diameters downstream and is illustrated in Figure 4.6. The vorticity field behind the rotor is then calculated using the velocity field. In Figure 4.6, the magnitude of the vorticity is sufficiently large that the trajectory of the tip vortices is clearly seen. The development of the wake is visualized, and as expected the wake convects downstream with the effect of forward speed.

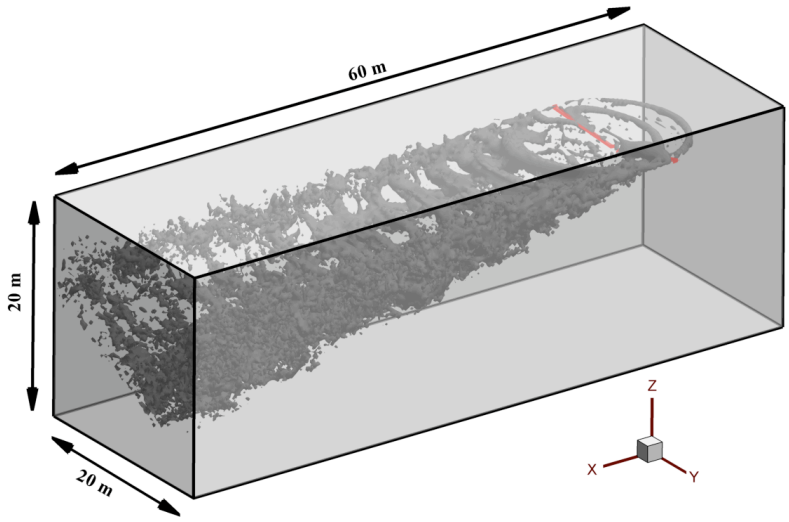

Figure 4.6 *Iso-vorticity surfaces obtained in the volume*

Figure 4.7 compares the iso-vorticity surfaces in the wake flow field of the UH-1H rotor in 60 knots and 80 knots forward flight after 10 rotor revolutions. The magnitude of the vorticity on the plotted surface is sufficiently large. Therefore, these surfaces can be used to illustrate the trajectories of the tip vortices, since the tip vortices have high vorticity. The asymmetry of the wake is visible and the high vorticity region is dominant on the advancing side of the rotor. The asymmetry between the advancing and retreating sides is more in 60 knots forward flight than 80 knots condition. Moreover, at 60 knots forward flight, the vorticity iso-surfaces are denser than the 80 knots forward flight condition. The mutual interactions between the individual vortex filaments cause distortion in the vortex positions. This is seen mostly in the z direction. This vertical distortion of the wake is stronger at low speed forward flight. This is illustrated in Leishman [2] by the smoke ejection experiment which was conducted to show the vortex locations in forward flight. As seen in Figure 4.7, the wake convects downstream with the freestream velocity. Therefore, the wake skew angle is more in 80 knots forward flight condition.

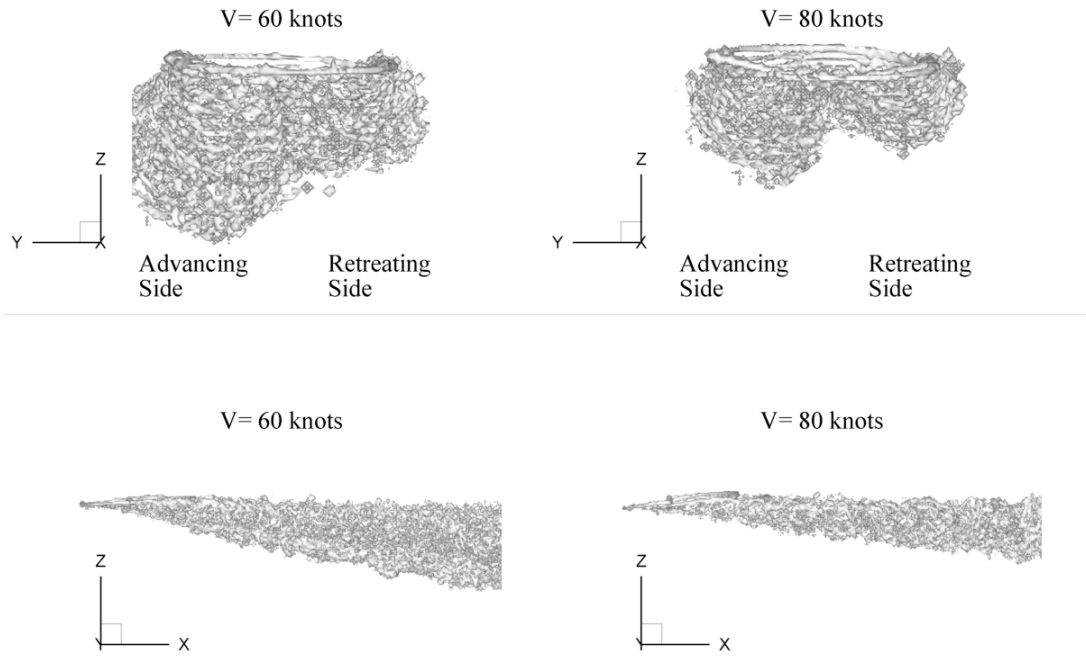

Figure 4.7 *Iso-vorticity surfaces obtained in the volume*

The effect of vortex core radius is investigated. The results are found to be sensitive to the selection of the vortex core size. The vortex core radius used in simulations affect the aerodynamic loads on the blades. Therefore, different vortex core sizes are tested in order to see the effects on the results (0.003m, 0.004m and 0.005m). A vortex core radius of 0.005m corresponds to 5% of the spanwise smallest blade panel, 0.07% of the rotor radius and 0.94% of the chord length. Szymendera [31] used a vortex core radius equal to 0.1% of the spanwise dimension of the smallest blade panel, in his analyses using free wake vortex lattice method.

Figure 4.8 and Figure 4.9 show the sensitivity of the computed value of the vertical force to the vortex core radius, in both hover and forward flight. In hover case, the predictions of vertical force using a vortex core radius of 0.005m were found to be the approximate result when compared to the maximum gross weight of the UH-1H helicopter (36000N). For 60 knots forward flight, the effect of core radius follows a similar trend. However, using the core radius values for hover results in a higher than expected vertical force in 60 knots forward flight. As in hover case, the result with a vortex core radius of 0.005m seems to be producing the best result for 60 knots forward flight. In addition to the

analyses with these three vortex core sizes, larger vortex core radius settings were examined to ensure if they provide a more accurate vertical force. However, the analyses with a vortex core radius of 0.006 m and larger, cause wake instabilities and do not provide reasonable results. Therefore, the interaction analyses at forward flight have been performed using a vortex core radius of 0.005m.

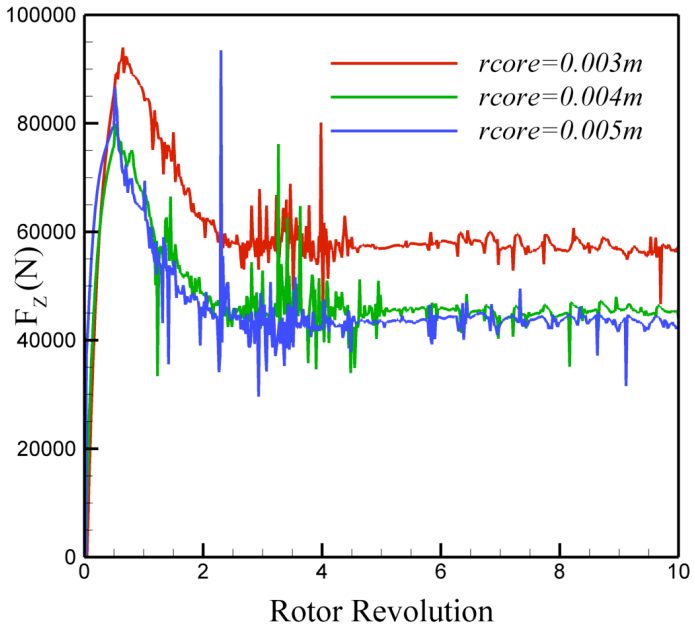

Figure 4.8 *Effect of vortex core radius on the total thrust coefficient for the UH-1H rotor in hover (Rankine model is used in these simulations)*

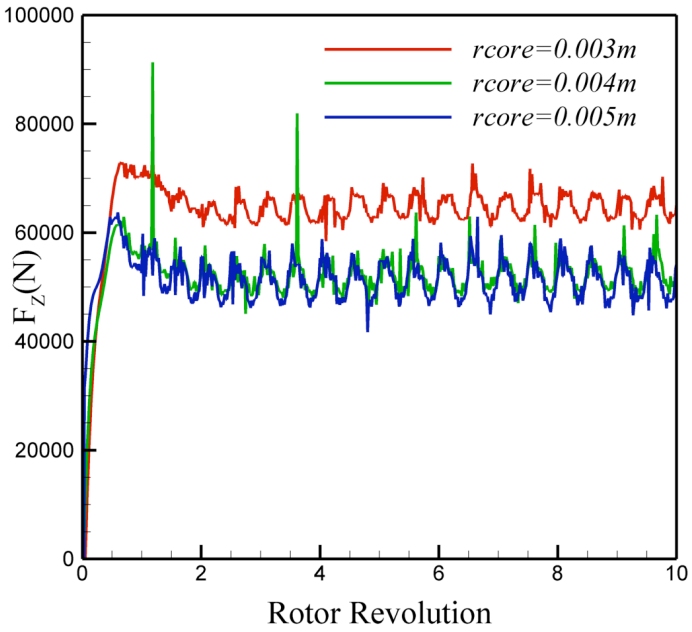

Figure 4.9 *Effect of vortex core radius on the total thrust coefficient for the UH-1H rotor in 60 knots forward flight condition (Rankine model is used in these simulations)*

4.4 UH-1H ROTOR-ROTOR INTERACTION SIMULATIONS

The focus of the current study is to investigate rotor-rotor aerodynamic interactions. For this purpose, two UH-1H rotors are simulated in forward flight. The analyses are performed using AeroSIM+ which is a 3-D unsteady vortex panel method potential flow solver based on a free wake methodology. The interaction scenarios, the characteristics of the wake flow and the effects on aerodynamic loads are all presented.

4.4.1 Interaction Scenarios

The investigation is performed for two UH-1H rotors, one flying downstream of the rotor in front. The intensity of the interactions and the resultant aerodynamic force and moments are sensitive to the relative position of the rear rotor. Therefore, the simulations are performed at ten different locations of the rear rotor as presented in Figure 4.10. In Case 1 (top row in Figure 4.10), the distance between the hub centers is 24.7 m, which corresponds to the case where the hub center of the rear rotor is 1 diameter away from

the tail of the front helicopter. In case 2 (bottom row in Figure 4.10), the distance between the hub centers is 32.0 m, in which the rear rotor is 1 additional radius away from the front rotor. In all cases the rear rotor is located slightly lower in z direction compared to the front rotor to make sure that it will be operating within the wake flow field.

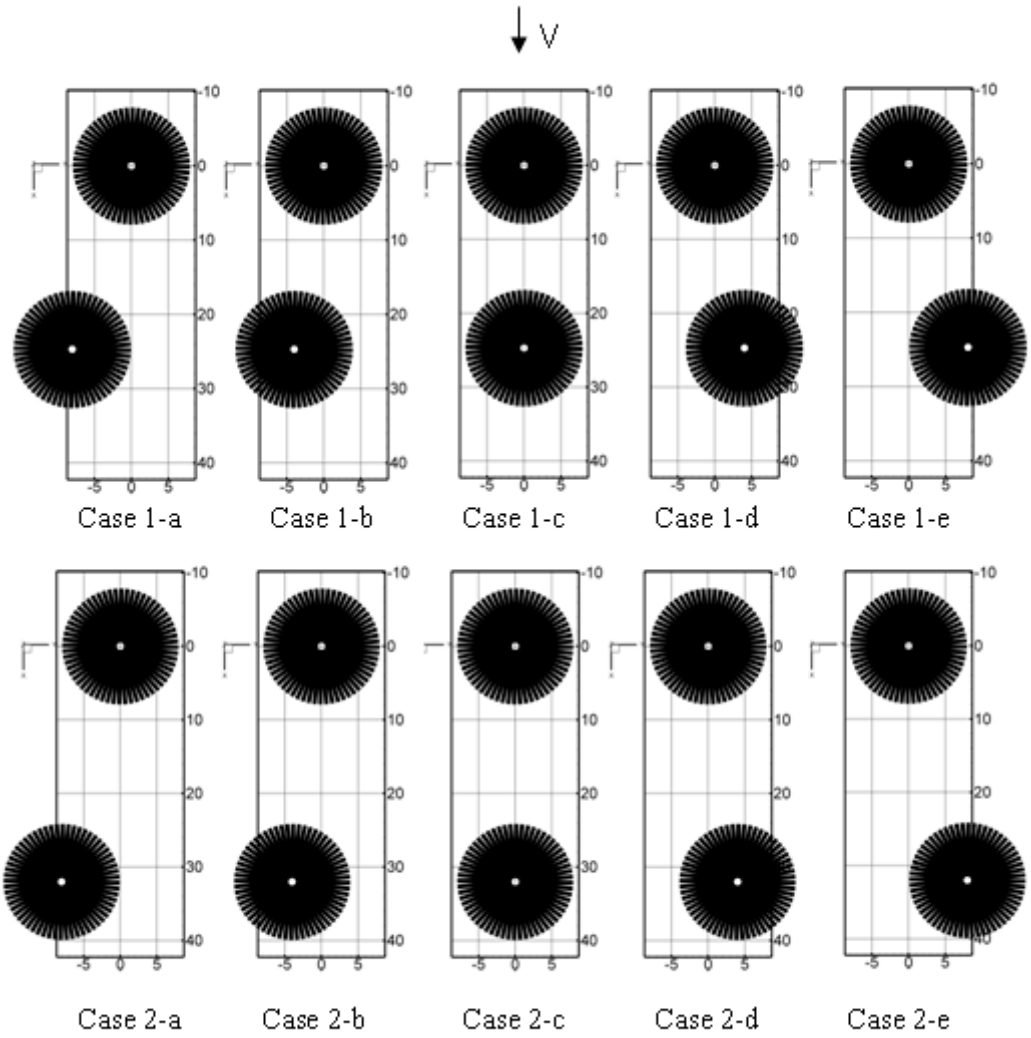

Figure 4.10 *Computational cases for interaction analyses between two UH-1H rotors: Case 1-a → Case 1-e(top row) show 5 different locations of the rear rotor in y direction when the difference between hub centers is 24.7m, Case 2-a → Case 2-e (bottom row) show 5 different locations of the rear rotor in y direction when the difference between hub centers is 32 m.*

4.4.2 Wake Flow Structure

The wake structure of case 1-c at 60 knots forward flight is illustrated in Figure 4.11 using iso-vorticity surfaces in the wake flow field after 10 rotor revolutions. The magnitude of the vorticity is sufficiently large that only tip and root vortices are visible. In this scenario the rear rotor is entirely operating within the complex vortical wake flow field of the front rotor interacting with the tip and root vortices shed from the front rotor. The complexity of wake structure for forward flight is clearly seen in the figures. The trajectory of the tip vortices and the development of the wake are compared in 60 knots and 80 knots forward flight conditions. The main rotor wake rolls-up into a pair of "super-vortices" or "vortex bundles" at the edges of advancing and retreating sides as defined in Leishman [2]. The super vortices are similar to the vortices trailing at the tips of a fixed wing. The super vortices in the wake of of UH-1H rotor can be seen in Figure 4.11 (a). The vortex roll up is bigger in 60 knots forward flight than those in 80 knots forward flight condition. As can be seen from Figure 4.11 (b), the iso-vorticity surfaces are denser in 60 knots forward flight. Moreover, these high vorticity regions are denser on the advancing sides. Blade-vortex interactions are seen in Figure 4.11 (b). The vortices impinge on the other blade near the tip region when operating in 60 knots. On the other hand, this interaction occurs near mid-span when operating in 80 knots. As can be seen from Figure 4.11 (c), the wake geometry not only convects below the rotor disk area as in hovering case, but also convects downstream with the freestream velocity. In 80 knots forward flight, the wake skew angle is higher than the 60 knots forward flight case. In forward flight, the wake is more complicated and asymmetrical. The asymmetry of the wake is visible in Figure 4.11 (d). The downwash produced by the super vortices is clearly seen in Figure 4.11 (d). As shown, the downwash is not symmetric due to the asymmetry of the flow field and dominant at the advancing side.

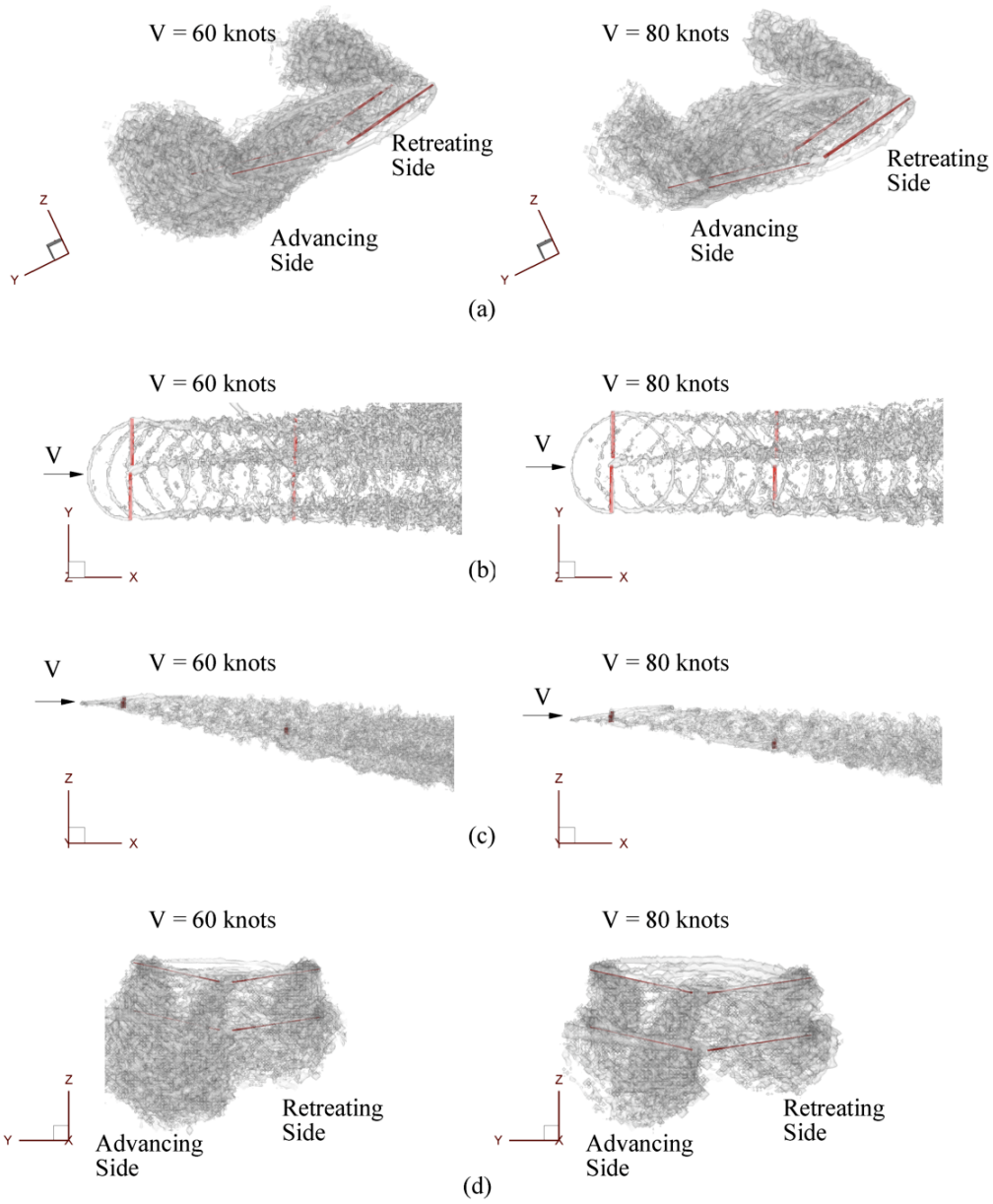

Figure 4.11 *Iso-vorticity surfaces showing tip and root vortex structures and the wake geometry behind UH-1H rotors at 60 knots and 80 knots forward flight after 10 rotor revolutions (Simulation of Case 1-c): (a) Isometric view, (b) Top view, (c) Side view, (d) Front view*

High vorticity region near the blade tips rolls up into concentrated dominant streamwise vortices. The resulting tip vortices have high swirl velocities along the lateral edges of the wake. Figure 4.12 shows constant x-planes for the case 1-c simulation in both 60 knots and 80 knots forward flight. Surfaces streamlines on these planes before and after

the rotors are shown. These streamlines illustrate the inflow through the rotor disk. As can be seen from the figure the tip vortices are a pair of counter rotating vortices at the tips. These are the "super vortices" as mentioned previously. The super vortices trail downstream along the lateral edges of the wake and are better illustrated in Figure 4.13.

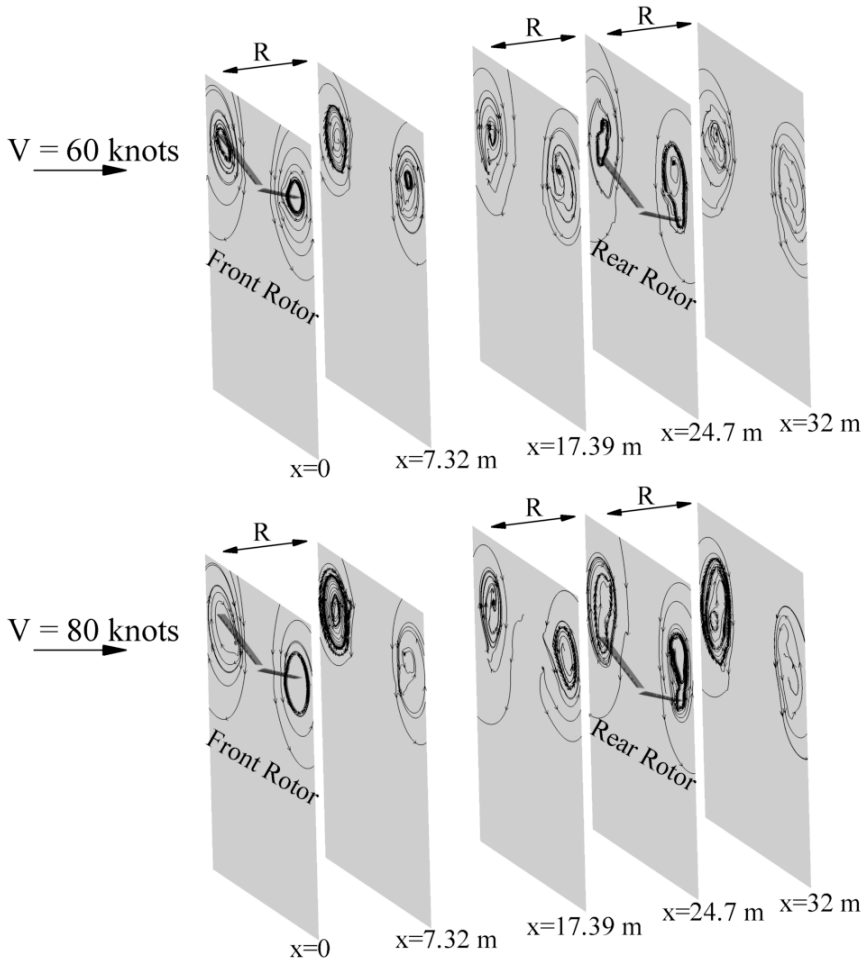

Figure 4.12 *Surface Streamlines of two UH-1H rotors operating at 60 knots and 80 knots forward flight after 10 revolutions (case 1c)*

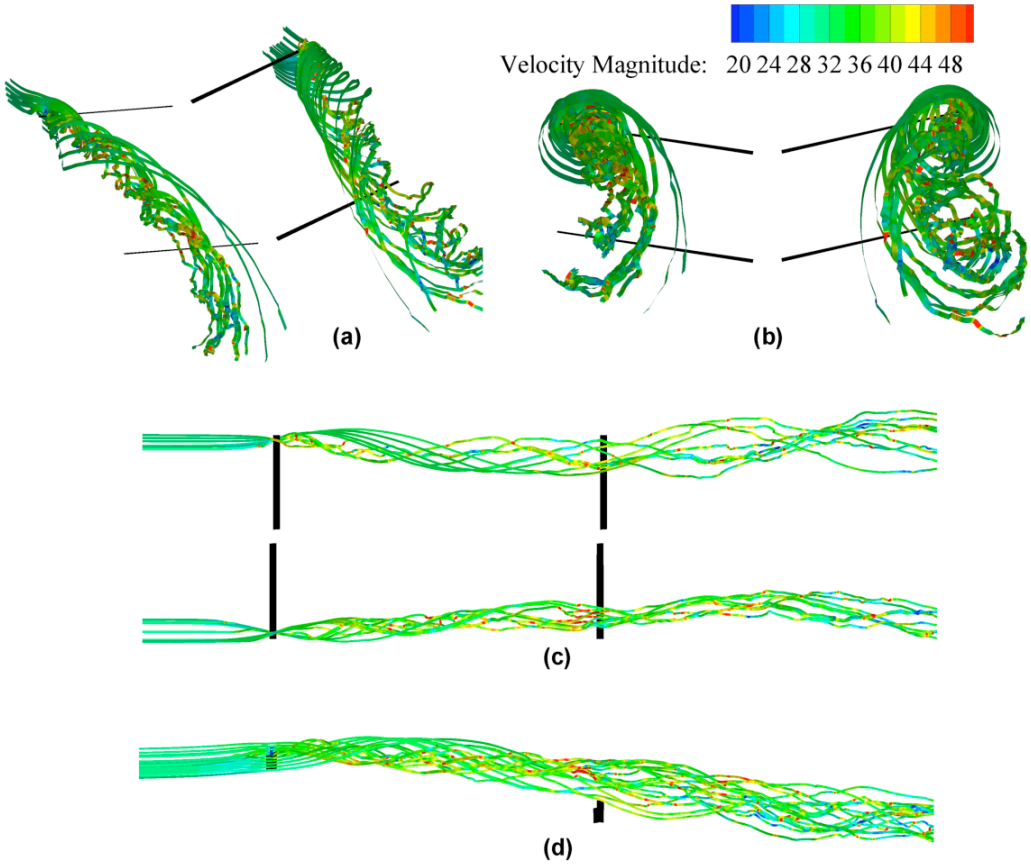

Figure 4.13 *Volume Streamlines of two UH-1H rotors operating at 60 knots after 10 revolutions (Case 1-c): (a) Isometric view, (b) Rear view, (c) Top view, (d) Side view*

Figure 4.13 shows four different views of volume streamlines. The trailing vortices at the tips are seen clearly in Figure 4.13 (a). Due to the asymmetric flow field, the streamlines differ at the advancing and retreating sides as shown in Figure 4.13 (b). The velocity increases in the wake so that a contraction occurs in the wake boundary. The contraction of the wake is seen in Figure 4.13 (c). The streamlines convect below the rotor as the wake develops. The rolled-up tip vortices of the front rotor impinge on the blades of the second rotor. Therefore, the induced velocity field of the rear rotor and the aerodynamic loads changes. These changes affect the performance characteristics, which are discussed later.

Figure 4.14 shows the velocity contours of case 1c simulation after 10 rotor revolutions for both 60 knots and 80 knots forward flight. In order to visualize the velocity fields of

both front and rear rotors, constant x planes are generated. Those planes are generated at the hub centers of the rotors. Moreover, the velocity contours at the planes before and after the rotors are also shown. The difference in the velocity contours of Figure 4.14 (a) and Figure 4.14 (b) is mainly due the freestream velocity. Because of the influence of the interactions, the velocity contours of the front rotor and rear rotor are different for both forward flight cases. As can be observed from the contours on 7.32 m plane, the flow is stable. After the front rotor, the velocity increases in the wake region. The rear rotor encounters a more complex and unsteady flow field with a higher freestream velocity when compared to the front rotor. In both figures, the asymmetry of the velocity field is evident. As seen from the velocity contours, the velocity magnitude at the retreating sides is smaller, as expected.

The vorticity distributions of the case 1-c simulation after 10 rotor revolutions are shown in Figure 4.15. The amount of circulation of the fluid flow is seen from the figure. As can be seen, the downwash generated by the tip vortices of rear rotor is more than the downwash generated by the tip vortices of front rotor. Moreover, the downwash is dominant at the advancing sides and is visible in the 60 knots simulation. In the far wake of 60 knots simulation, the effect of super vortices is clearly seen. The difference in the vortex strengths of the front rotor and the rear rotor is more in 60 knots forward flight condition. The vortex strengths affect the lift distribution. Therefore, the decrement in thrust of the rear rotor while operating at 60 knots forward flight is more than the 80 knots condition.

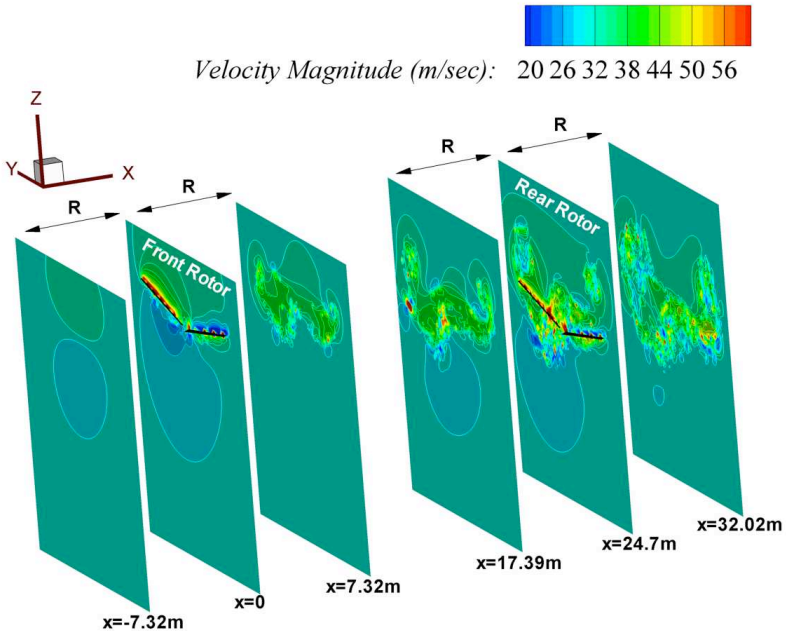

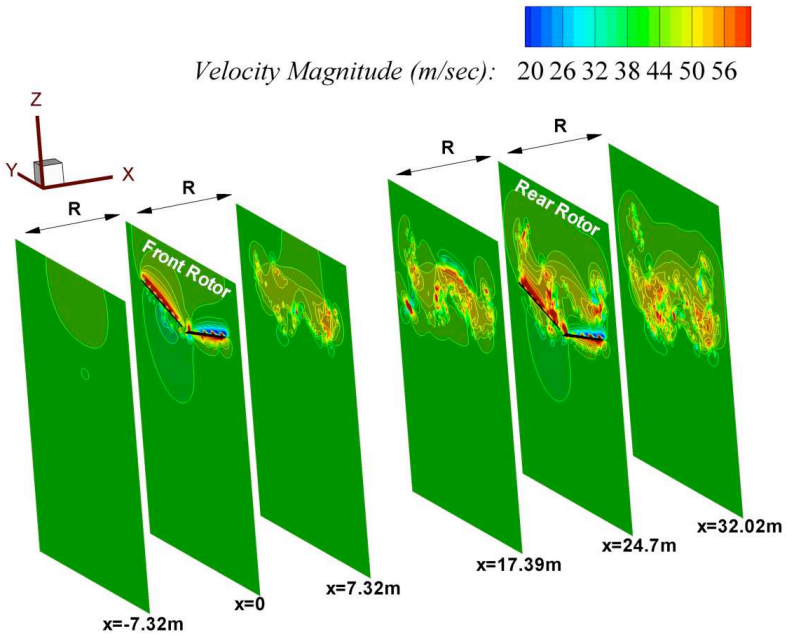

Figure 4.14 *Velocity contours after 10 revolutions (Case 1-c): (a) 60 knots, (b) 80 knots*

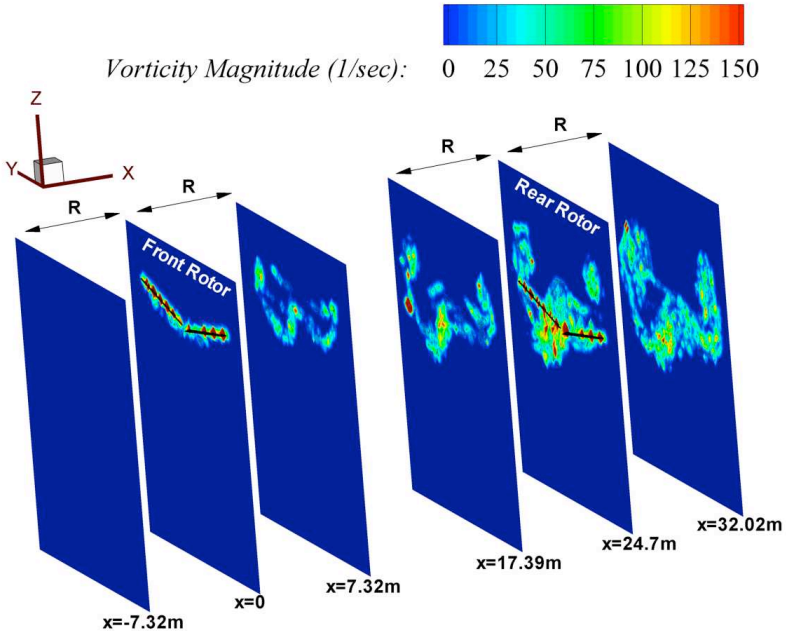

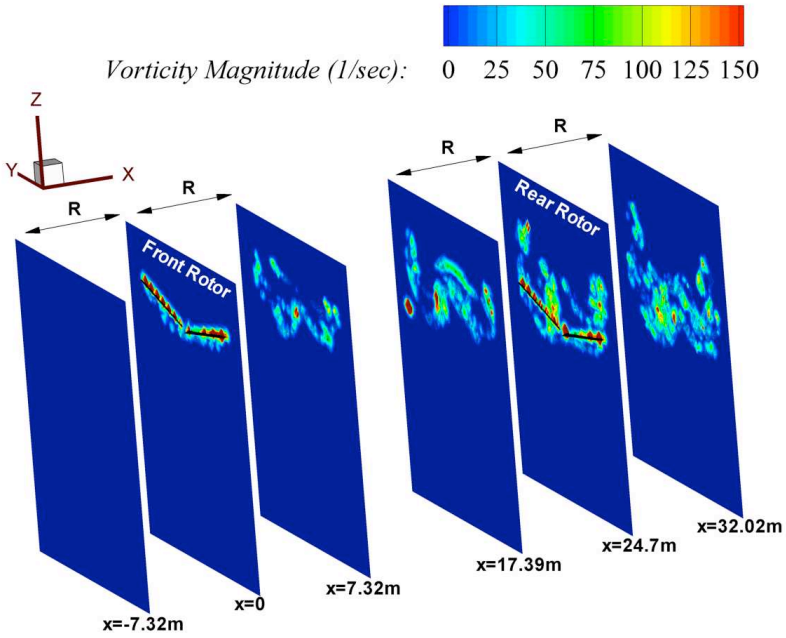

Figure 4.15 *Vorticity contours after 10 revolutions (Case 1-c): (a) 60 knots, (b) 80 knots*

Figures 4.16, 4.17 and 4.18 show the vorticity distributions of case 1c simulation after 10 rotor revolutions for both 60 knots and 80 knots forward flight. The vorticity distributions are plotted along the lateral edges of the wake in order to be able to illustrate the asymmetry of the downwash produced by the vortices. Trailing of the vortices to the downstream is visible in all three figures. Due to the mutual interactions between the individual vortex filaments, the vertical distortion of the wake is strong at low speed forward flight [2]. As can be seen from the figures, the distortion is much more at 60 knots forward flight.

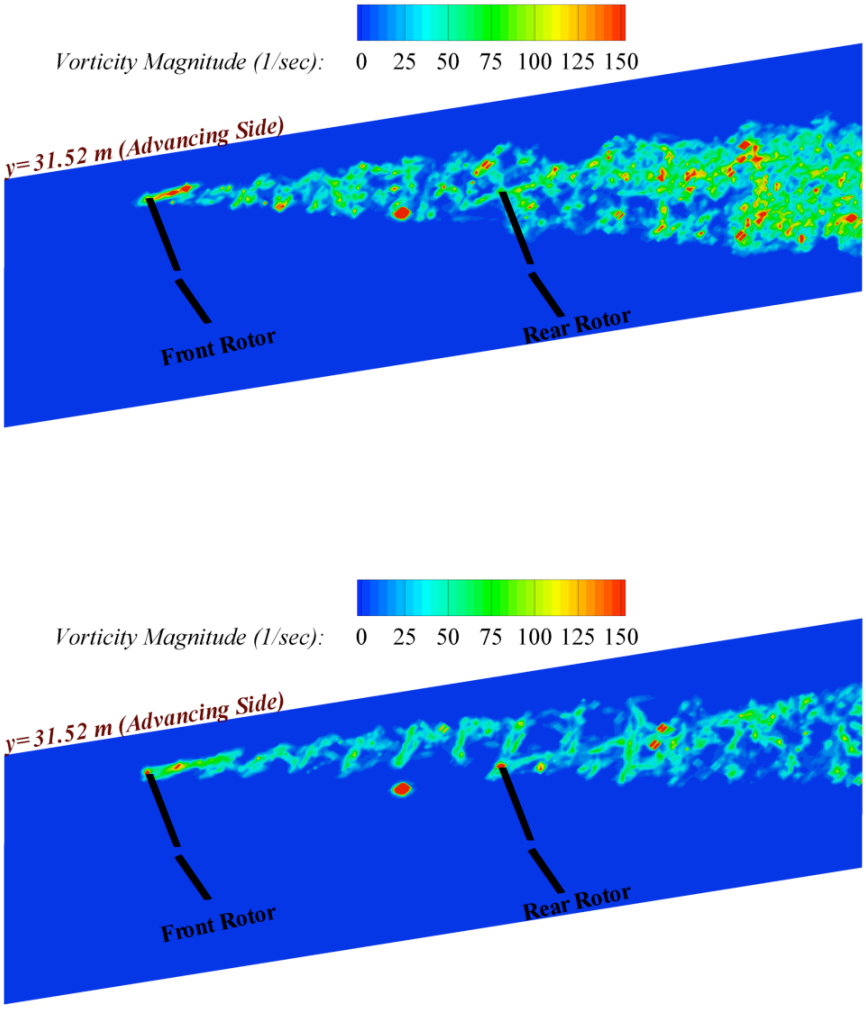

Figure 4.16 *Vorticity contours after 10 revolutions at y=31.52 m plane (Case 1-c): (a) 60 knots, (b) 80 knots*

In Figure 4.16, the vorticity distribution is shown along the advancing side. Figure 4.16(a) represents the distribution for 60 knots forward flight, whereas Figure 4.16(b) represents the distribution for 80 knots forward flight condition. Figure 4.17 shows the vorticity distribution along the retreating side. When the distributions at advancing and retreating sides are compared, the downwash of the vortices and the distortion in the wake are smaller at the retreating side. Figure 4.18 shows the vorticity distribution along the hub center. The distribution shows the root vortices which are also a dominant feature in the wake. As can be seen in Figure 4.18, the root vortices are dominant near the hubs of front and rear rotors.

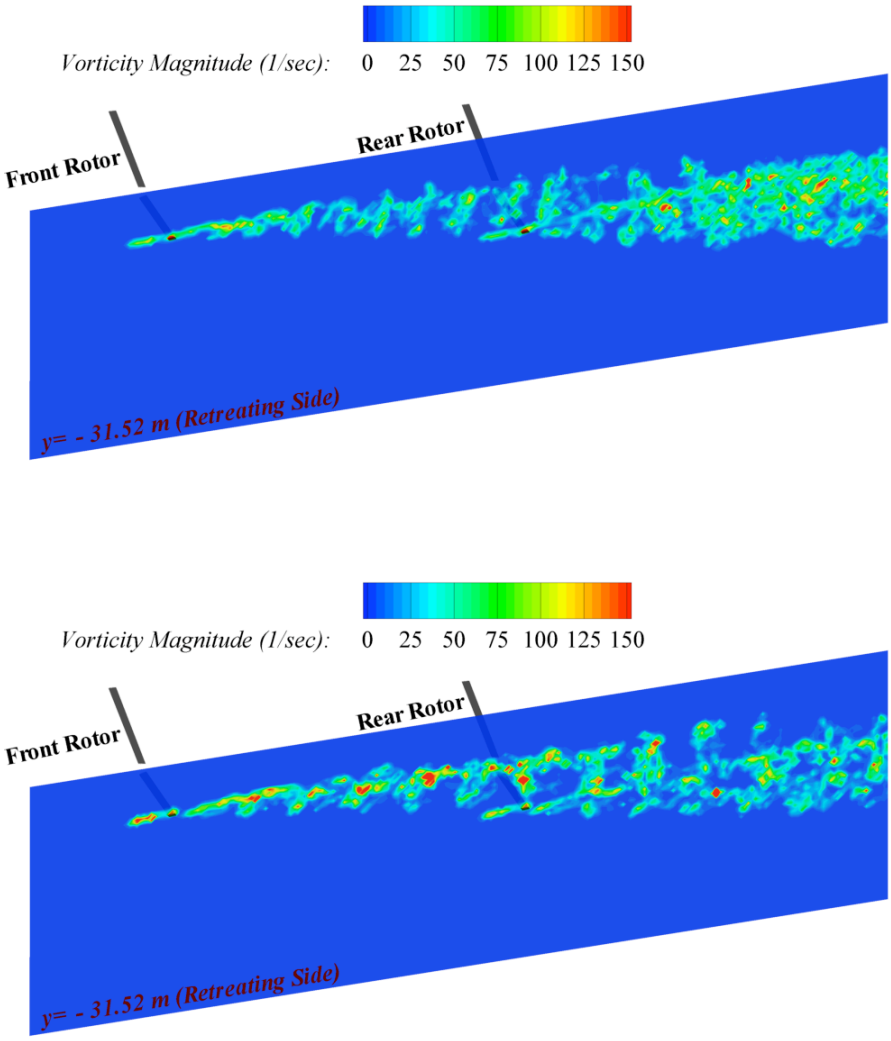

Figure 4.17 *Vorticity contours after 10 revolutions at y=-7.3152 m plane (Case 1-c): (a) 60 knots, (b) 80 knots*

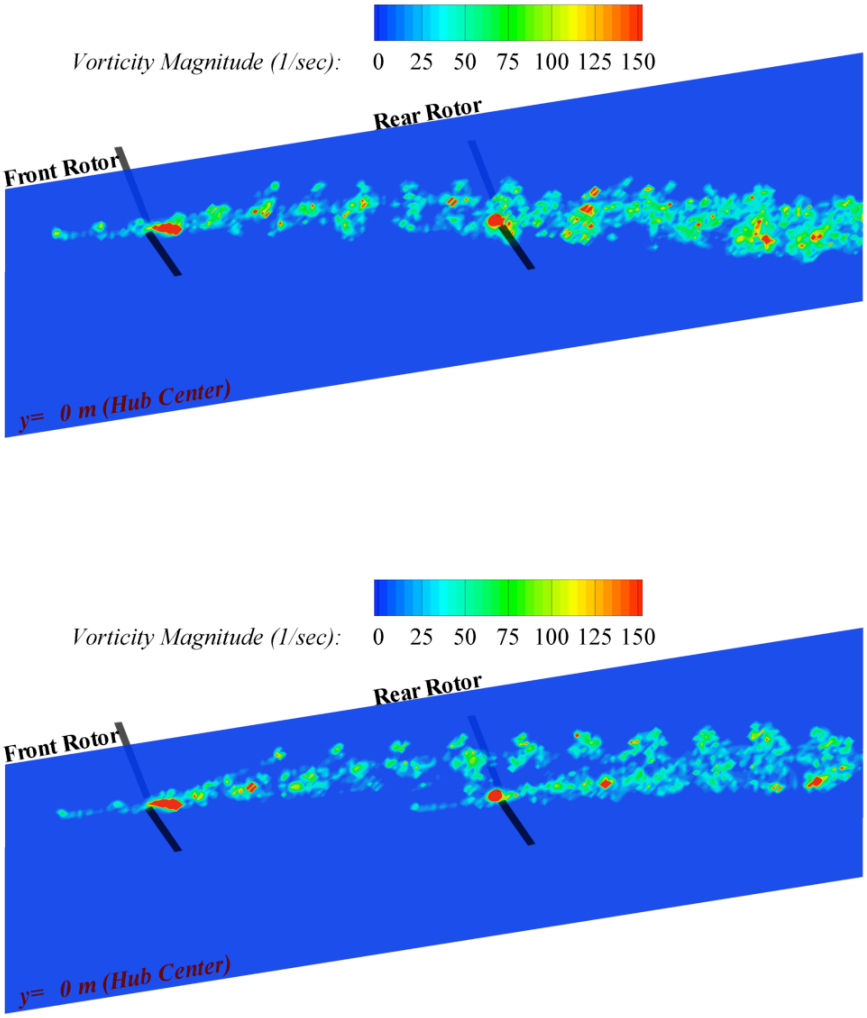

Figure 4.18 *Vorticity contours after 10 revolutions at y=0 plane (Case 1-c): (a) 60 knots, (b) 80 knots*

4.4.3 Effects on Aerodynamic Loads

The aerodynamic interactions between the two rotors affect the performance characteristics. As a part of the computation, time histories of all forces (F_X, F_Y, F_Z) and all moments (M_X, M_Y, M_Z) are calculated. Figures 4.19, 4.20, 4.21 and 4.22 show the time history of only the vertical force (F_Z) for both the rear and the front rotor over ten rotor revolutions. Vertical forces of all the cases, presented in Figure 4.10, are investigated when the rotors are operating at 60 knots and 80 knots forward flight. For Case 1-c, where the interactions are most severe, there's significant drop in thrust both

for 60 knots as well as 80 knots forward flight cases for the rear rotor. The thrust reduction at 60 knots seems to be slightly higher than the 80 knots forward flight case. Due to the asymmetric character of the front rotor wake, force variations differ depending on the lateral location of the rear rotor. When the rear rotor is operating at the advancing side of the front rotor, the reduction in the vertical force is more than when it is operating at the retreating side. The thrust reduction is not severe when the rear rotor is operating at the retreating side of the front rotor's tip region (Cases 1-a). The effect of the distance between the rotor hubs is seen in Figures 4.19 and 4.20 for 60 knots forward flight. For the 80 knots forward flight case, Figures 4.21 and 4.22 show the time histories of the vertical force. The plots show that the decrease in thrust is visible after 4 rotor revolutions when the rotors are operating at 60 knots and the distance between the rotor hubs is 24.7 m. For the case when the distance between the hubs is increased to 32 m, the thrust of the rear rotor starts to decrease after 5 rotor revolutions. Figure 4.21 shows that, thrust starts to decrease after three rotor revolutions because the wake develops rapidly when compared to the 60 knots condition. Figures 4.23, 4.24, 4.25 and 4.26 show the time history of only the yawing moment (M_Z) for both the rear and the front rotor over ten rotor revolutions. Yawing moment of all the cases, presented in Figure 4.10, are investigated when the rotors are operating at 60 knots and 80 knots forward flight. The yawing moments of front and rear rotor show similar trends in all cases and the mean of the moments are close.

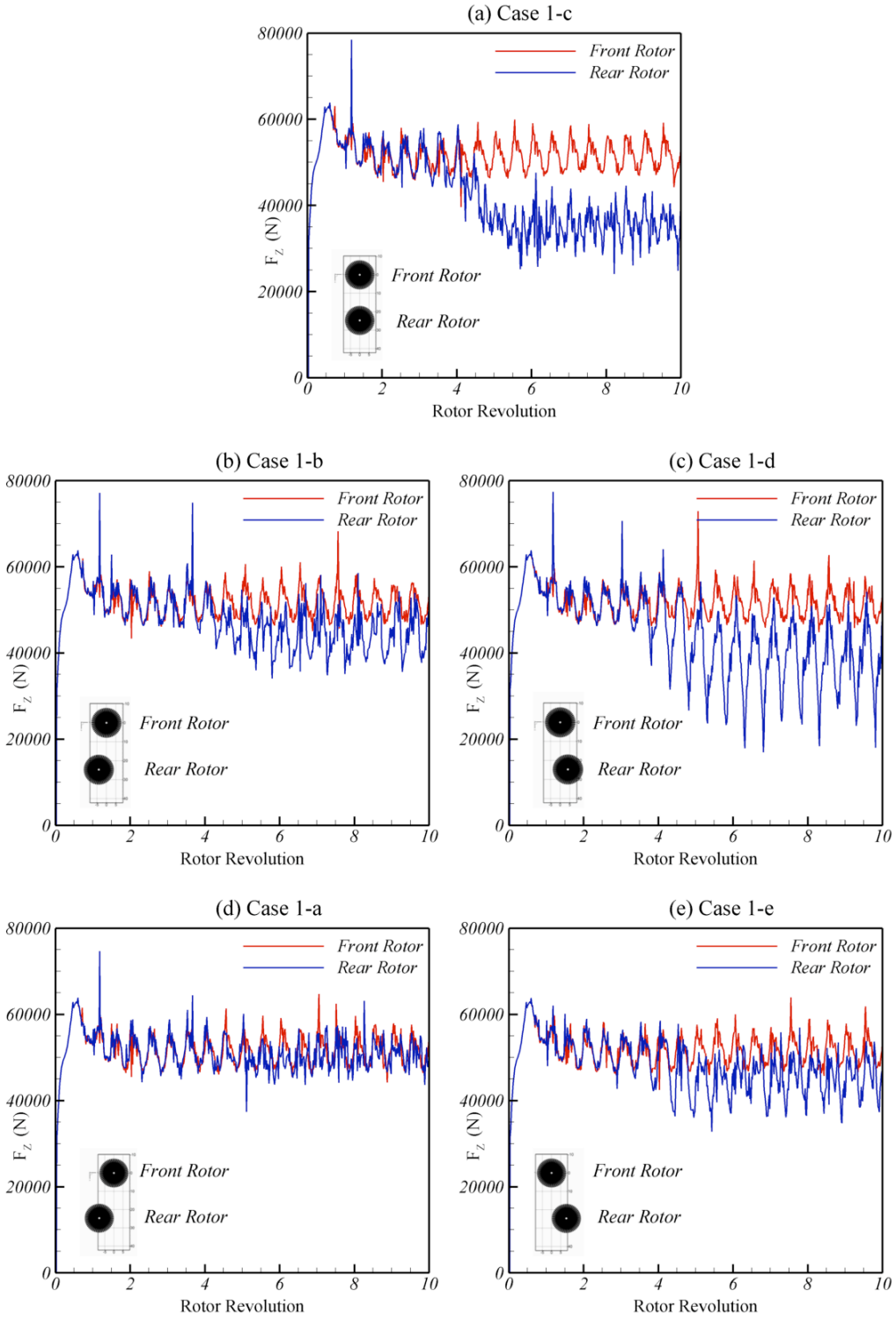

Figure 4.19 *Vertical force (F_Z) variations for 10 rotor revolutions in 60 knots when the distance between the hub centers is 24.7 m (a) case 1c (b) case 1b (c) case 1d (d) case 1a (e)case 1e (The cases are described in Figure 4.10)*

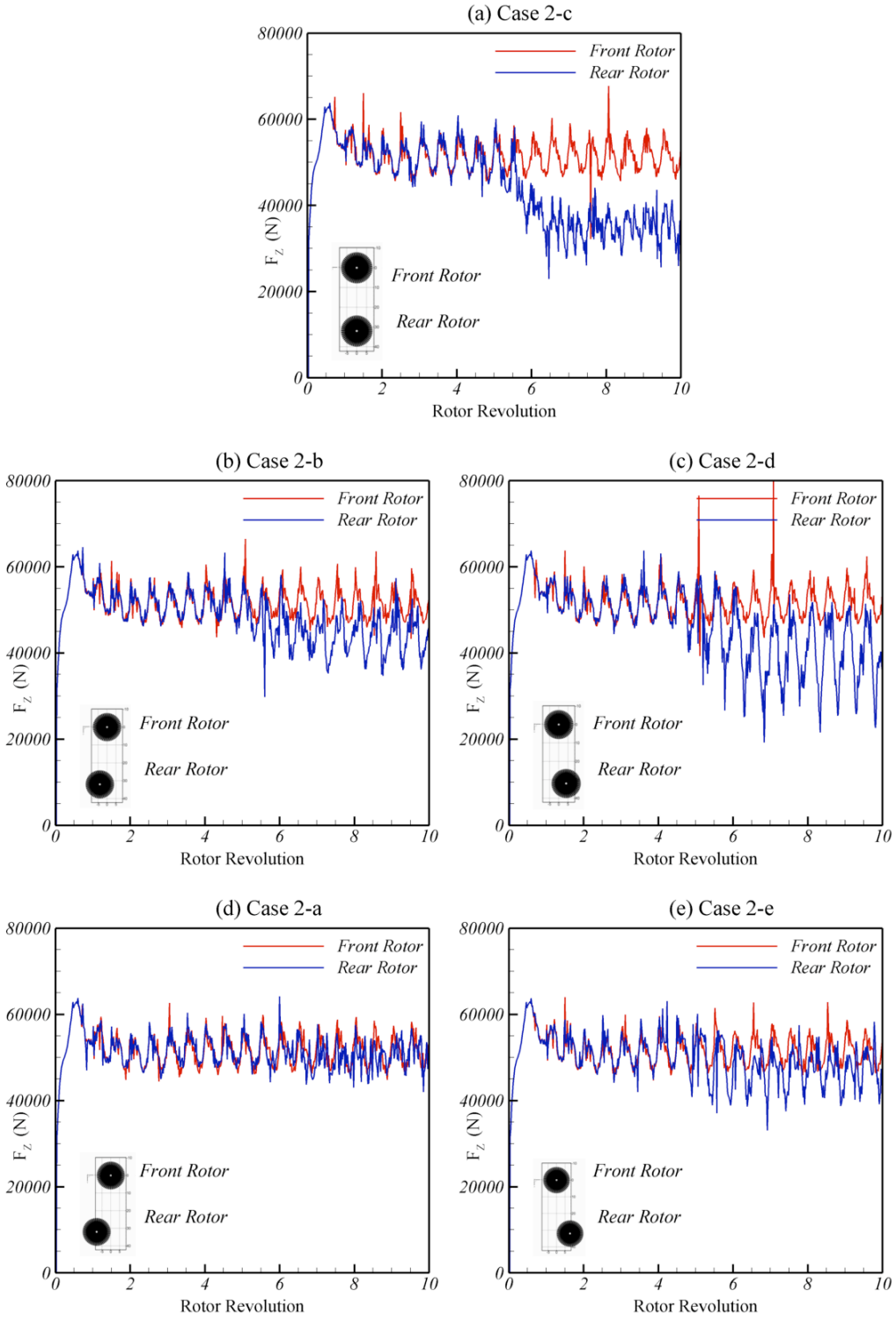

Figure 4.20 *Vertical force (F_Z) variations for 10 rotor revolutions in 60 knots when the distance between the hub centers is 32 m (a) case 2c (b) case 2b (c) case 2d (d) case 2a (e)case 2e (The cases are described in Figure 4.10)*

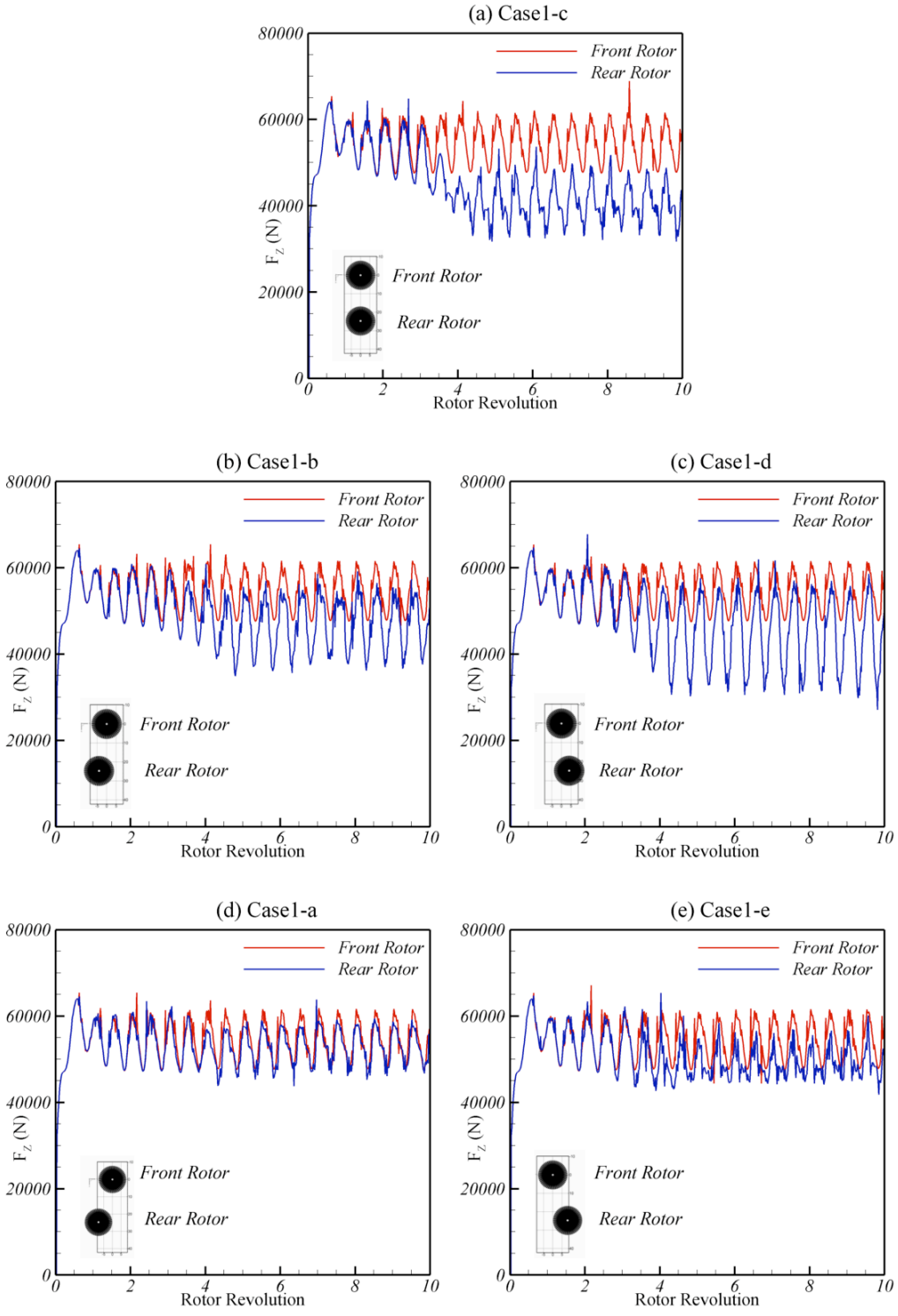

Figure 4.21 *Vertical force (F_Z) variations for 10 rotor revolutions in 80 knots when the distance between the hub centers is 24.7 m (a) case 1c (b) case 1b (c) case 1d (d) case 1a (e)case 1e (The cases are described in Figure 4.10)*

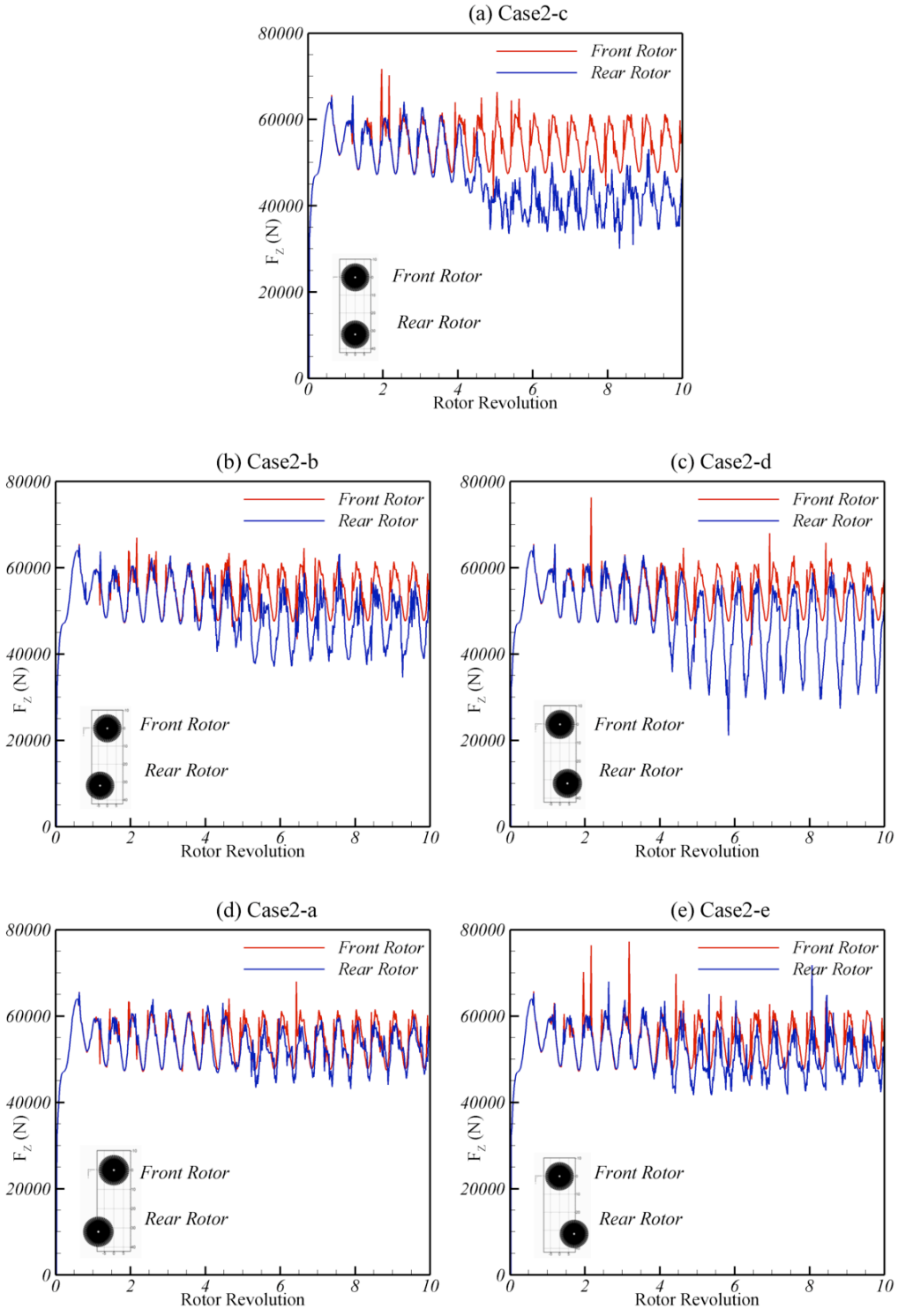

Figure 4.22 *Vertical force (F_Z) variations for 10 rotor revolutions in 80 knots when the distance between the hub centers is 32 m (a) case 2c (b) case 2b (c) case 2d (d) case 2a (e)case 2e (The cases are described in Figure 4.10)*

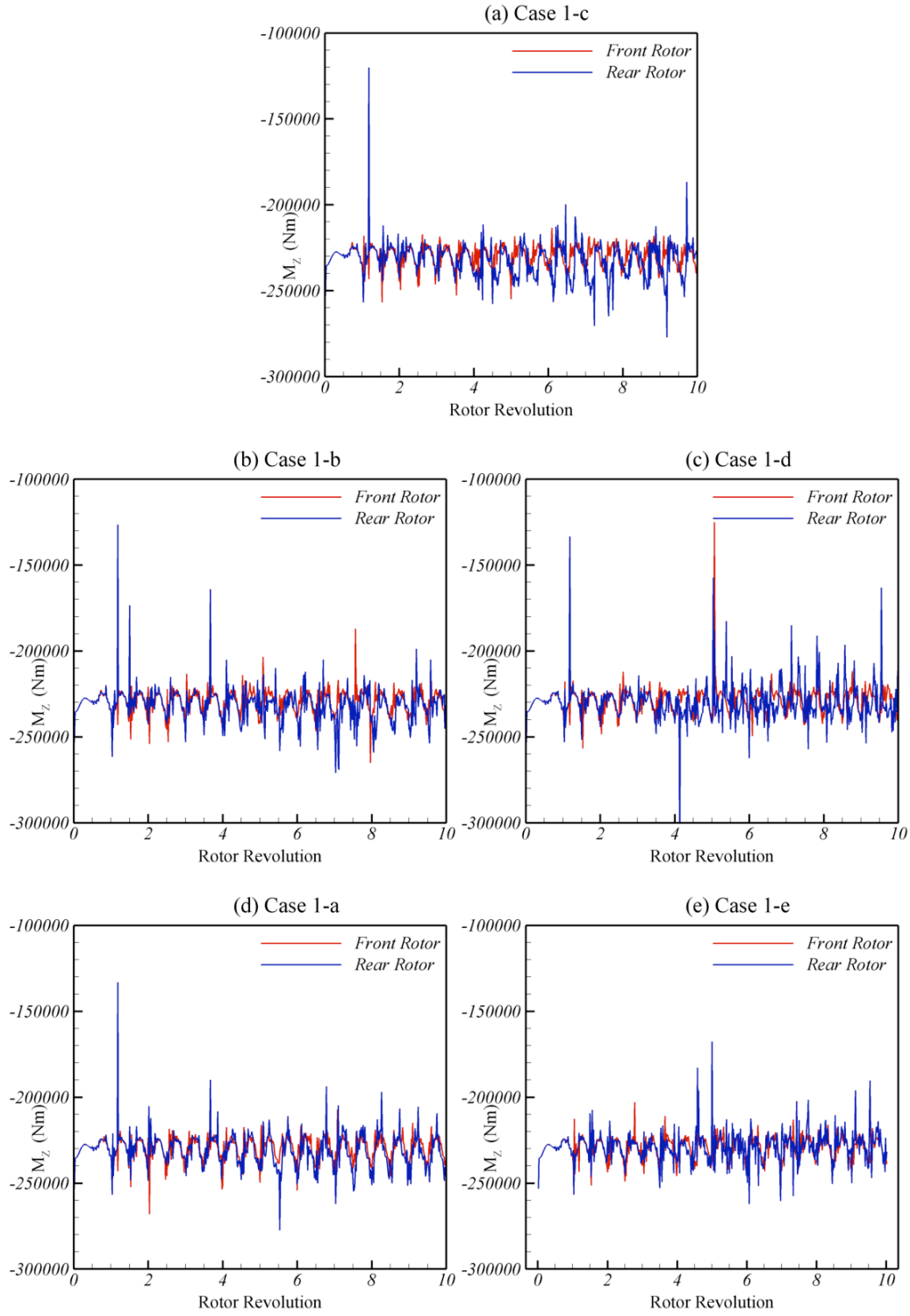

Figure 4.23 *Yawing moment (M_Z) variations for 10 rotor revolutions in 60 knots when the distance between the hub centers is 24.7 m (a) case 1c (b) case 1b (c) case 1d (d) case 1a (e)case 1e (The cases are described in Figure 4.10)*

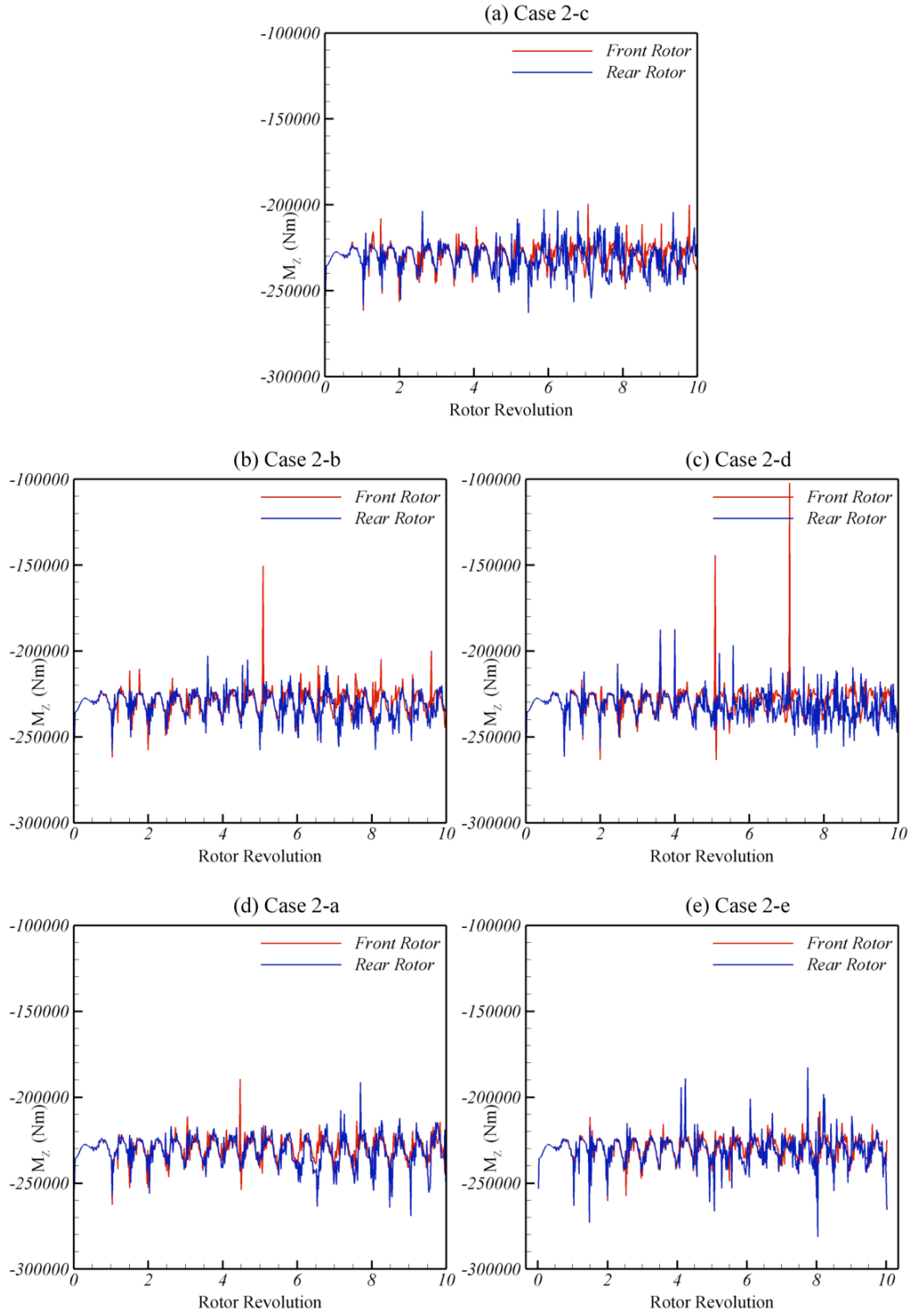

Figure 4.24 *Yawing moment (M_Z) variations for 10 rotor revolutions in 60 knots when the distance between the hub centers is 32 m (a) case 2c (b) case 2b (c) case 2d (d) case 2a (e)case 2e (The cases are described in Figure 4.10)*

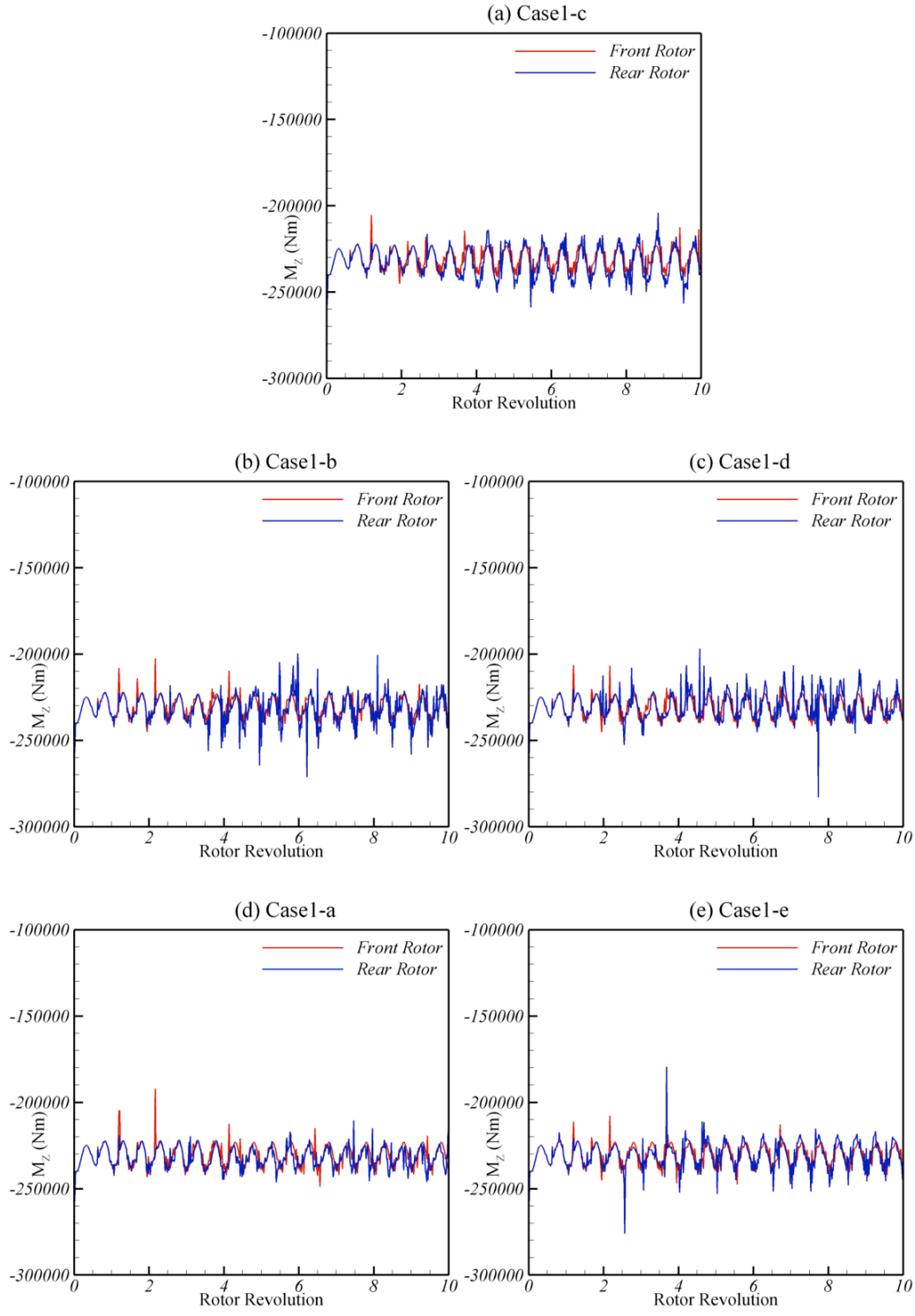

Figure 4.25 *Yawing moment (M_Z) variations for 10 rotor revolutions in 80 knots when the distance between the hub centers is 24.7 m (a) case 1c (b) case 1b (c) case 1d (d) case 1a (e)case 1e (The cases are described in Figure 4.10)*

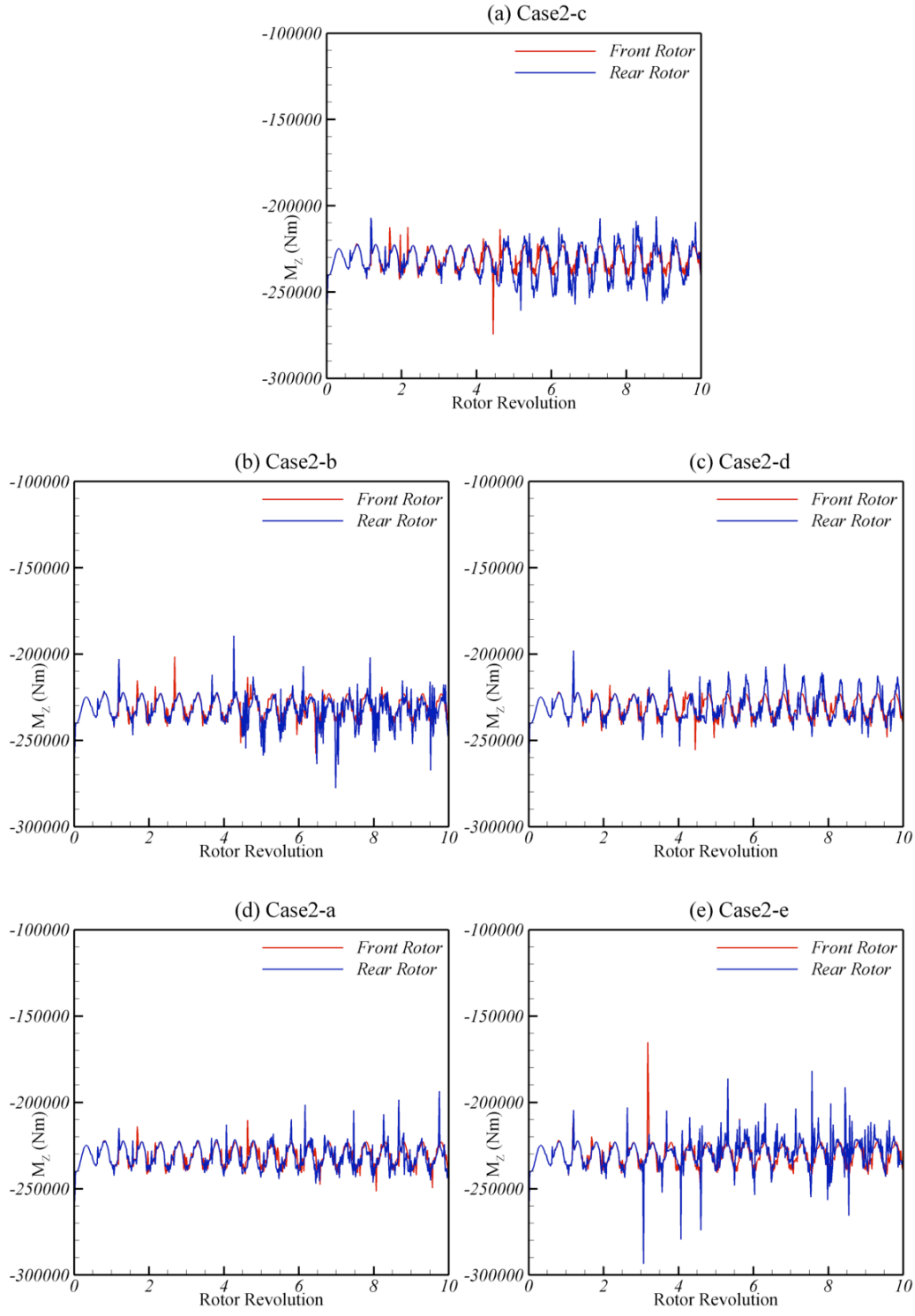

Figure 4.26 *Yawing moment (M_Z) variations for 10 rotor revolutions in 80 knots when the distance between the hub centers is 32 m (a) case 2c (b) case 2b (c) case 2d (d) case 2a (e)case 2e (The cases are described in Figure 4.10)*

Using the time histories of the computed forces and moments average values are calculated using the periodic data obtained after about 5 revolutions. After having the arithmetical mean of all the forces and moments for both front and rear rotors, the amount of change in the rear rotor with respect to the front rotor is calculated using

$$\Delta F = \frac{F_{rear} - F_{f\,ront}}{F_{f\,ront}} x\,100 \tag{4.9}$$

$$\Delta M = \frac{M_{rear} - M_{f\,ront}}{M_{f\,ront}} x100 \tag{4.10}$$

Figures 4.27 and 4.28 show the changes in the rear rotor's performance characteristics in terms of the forces (F_X, F_Y, F_Z) and moments (M_X, M_Y, M_Z). The rear rotor operates in the wake of the front rotor. The first columns show the results of 60 knots forward flight condition. The results of 80 knots forward flight simulations are presented in the second columns. In each plot, both the effect of the proximity of the rotors and the lateral position of the rear rotor are discussed (case 1 and case 2 simulations which are previously described in Figure 4.10). As can be seen in Figures 4.27 and 4.28, case 1 and case 2 simulations produce similar results. The dissimilarities occur due to the intensity of the interactions which differs by the longitudinal distance between the hub centers.

As can be seen in Figure 4.27, F_X of the rear rotor increases with respect to the front rotor. Due to the interactions with the front rotor wake, the velocity field of the rear rotor changes as seen in Figure 4.14. The rear rotor blades encounter a higher and a complex flow field. The maximum increment in F_X is seen in case 1d. Nearly in all cases F_Y of the rear rotor decreases. In 60 knots forward flight the maximum decrease is seen for case 1c simulation. On the other hand, in 80 knots forward flight the maximum decrease is seen for case 1d simulation. The vertical component of the force, F_Z, shows a degradation due to the influence of the front rotor wake. For both 60 knots and 80 knots forward flight conditions, maximum decrease occurs in case 1c simulation where the interactions are severe. The decrements are more when the rear rotor is operating at the advancing side rather than the retreating side.

Figure 4.28 shows the amount of changes in moments of the rear rotor. The rolling moment (M_X) decreases in case 1a, 1b and 1c simulations. The amount of decrement is more when the rotors are operating in 80 knots forward flight condition. When the rear rotor operates at the starboard of the front rotor the rolling moments increase. The pitching moment (M_Y) decreases at case 1a, 1b and 1c simulations in 80 knots forward flight. Maximum decrease is seen in case 1a simulation. The rolling moment of the rear rotor increases when operating at the starboard side of the front rotor. Maximum increment is seen in case 1e simulation. On the other hand, at 60 knots forward flight the rolling moment decreases 2% in case 1d and 12% in case 2d. There is an increment in pitching moment in case 1e and case 2e simulations. The yawing moment of the rear rotor slightly changes in all simulation cases for both 60 knots and 80 knots forward flight as seen in Figure 4.28.

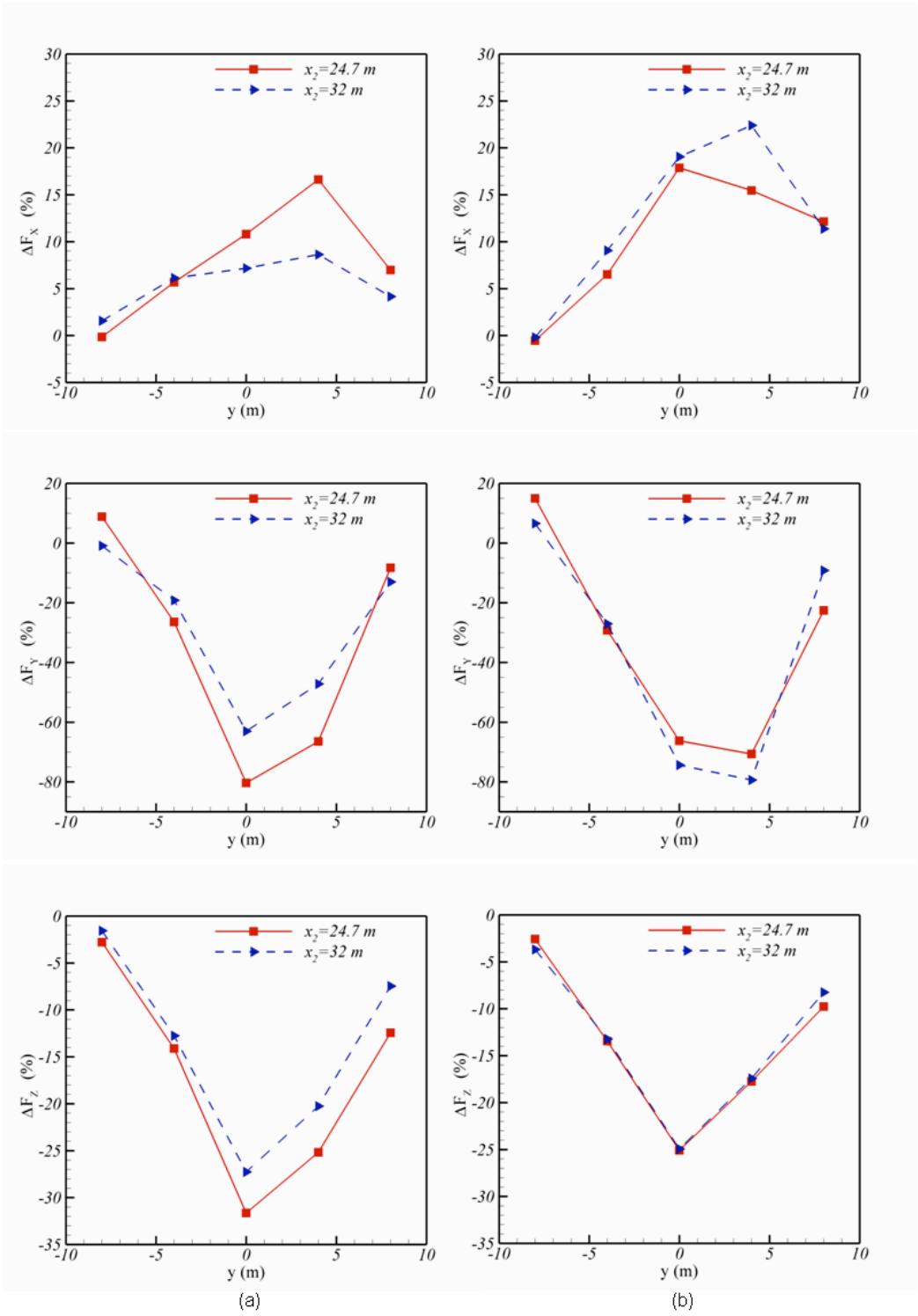

Figure 4.27 *Percentage change in forces of the rear rotor with respect to the front rotor (a) at 60 knots (b) 80knots*

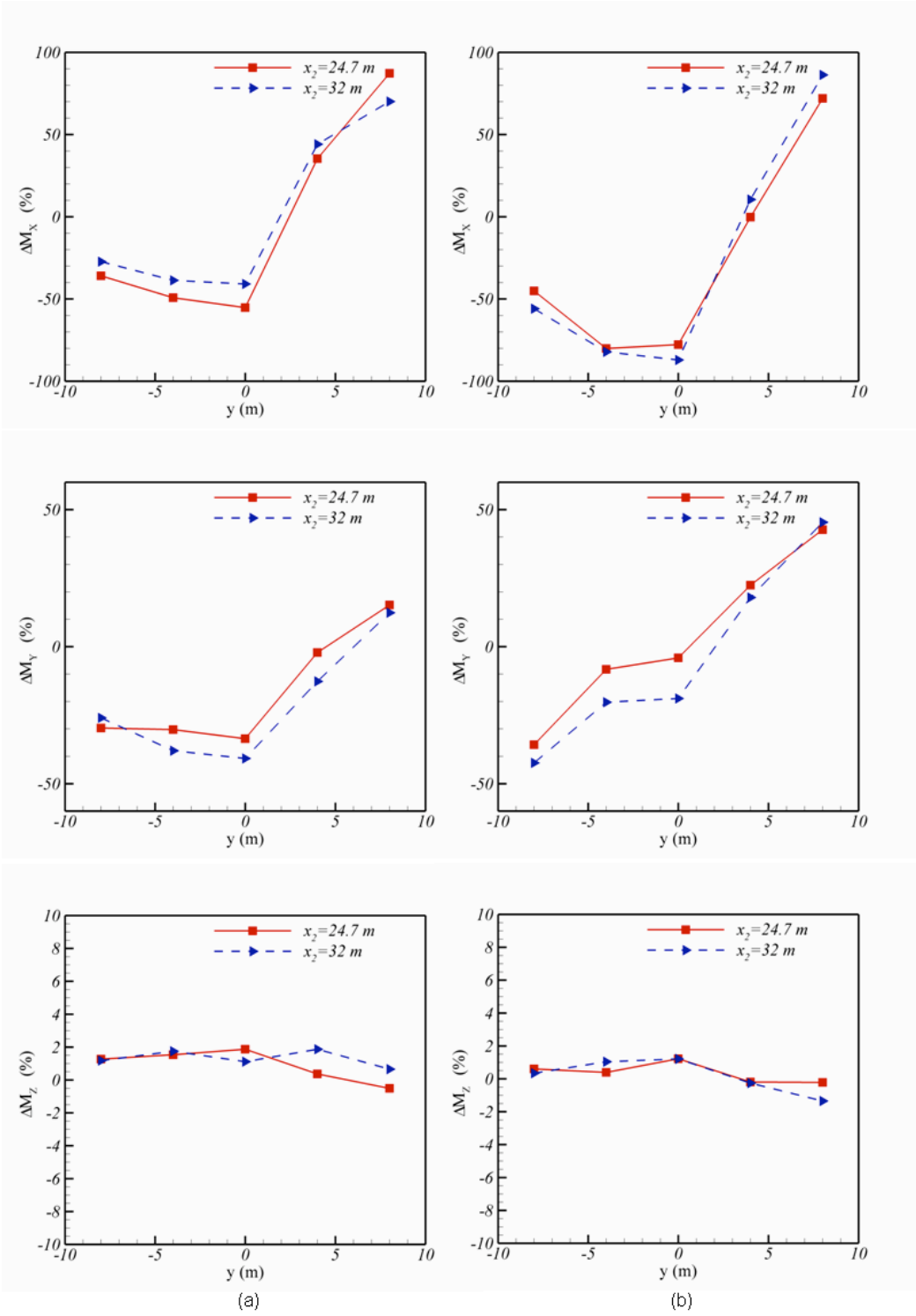

Figure 4.28 *Percentage change in moments of the rear rotor with respect to the front rotor (a) at 60 knots (b) 80knots*

The frequency analysis of force and moment oscillations is performed. The rotational speed of the UH-1H rotor is 324 rpm. Therefore, the rotational and the blade passing frequencies are 5.4 Hz and 10.8 Hz, respectively (UH-1H rotor has two blades). Knowing that the blade advances 6^0 at each time step, and therefore, one revolution is completed in 60 time steps (i.e. 60 sample solutions are obtained in one revolution) the sampling rate is calculated as

$$60\frac{sample}{rev}x\frac{324}{60}\frac{rev}{\sec}=324Hz \tag{4.11}$$

The frequency axis extends from zero to half the sampling rate, and therefore 160 Hz was used in performing Fourier transforms. For a given signal, the power spectrum gives a plot of the portion of a signal's power within the described frequencies. Figure 4.29 shows the frequency analysis of the forces in case 1c simulation. The computed performance data showed that in vertical force (F_Z) of the front rotor, the dominant peak occurs at the blade passing frequency which is 10.8 Hz. The main reason is that the interactions have little influence on the performance characteristics of the front rotor. There are also peaks at the harmonics. However, due to the effects of interactions, the rear rotor has a dominant peak at the 21.6 Hz, two times the blade passing frequency. It means that the rear rotor is also under the influence of the blade passing frequency of the front rotor. There are also some peaks at the frequencies that are not the harmonics of the blade passing frequency. F_X and F_Y of both front and rear rotors show similar characteristics in terms of frequency analysis. The dominant peaks are seen at the blade passing frequencies. So in terms of F_X and F_Y oscillations, rear rotor seems to be minimally affected by the front rotor.

Figure 4.30 shows the frequency analysis of the moments in case 1c simulation. The rolling moments, M_X, of the front and rear rotors have a dominant peak at the blade passing frequency. Smaller peaks occur at 21.6 Hz. The pitching moment, M_Y, is affected by the interactions and the rear rotor has a dominant peak at 21.6 Hz. The frequency analysis of the pitching moment of the rear rotor shows a similar result with the vertical force. As for the yawing moment, M_Z, both the front and rear rotors have a dominant peak at the blade passing frequency. Although, the affects of interactions are seen in the rear rotor, they do not dominate the blade passing frequency.

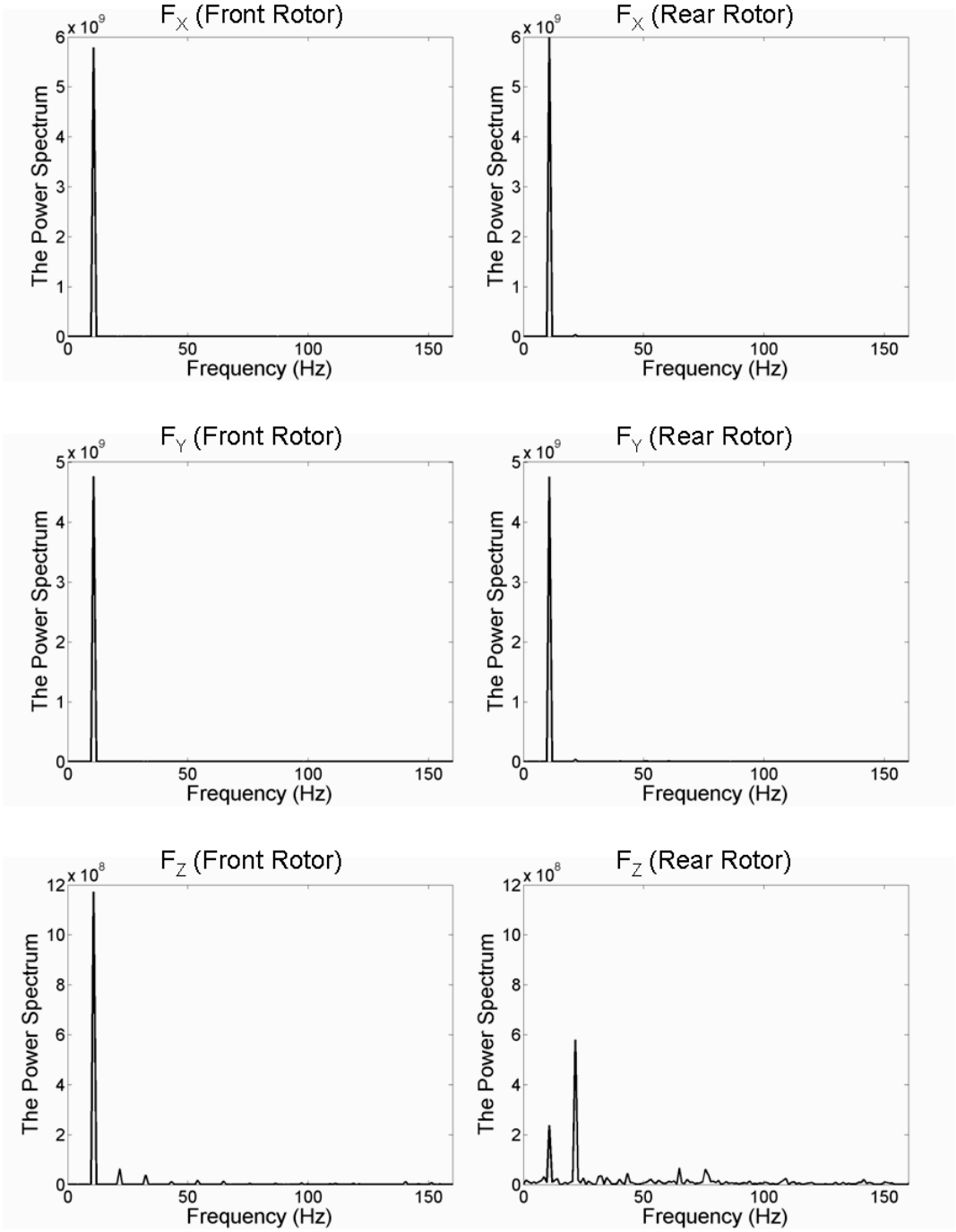

Figure 4.29 *Frequency analysis of forces in case 1c simulation*

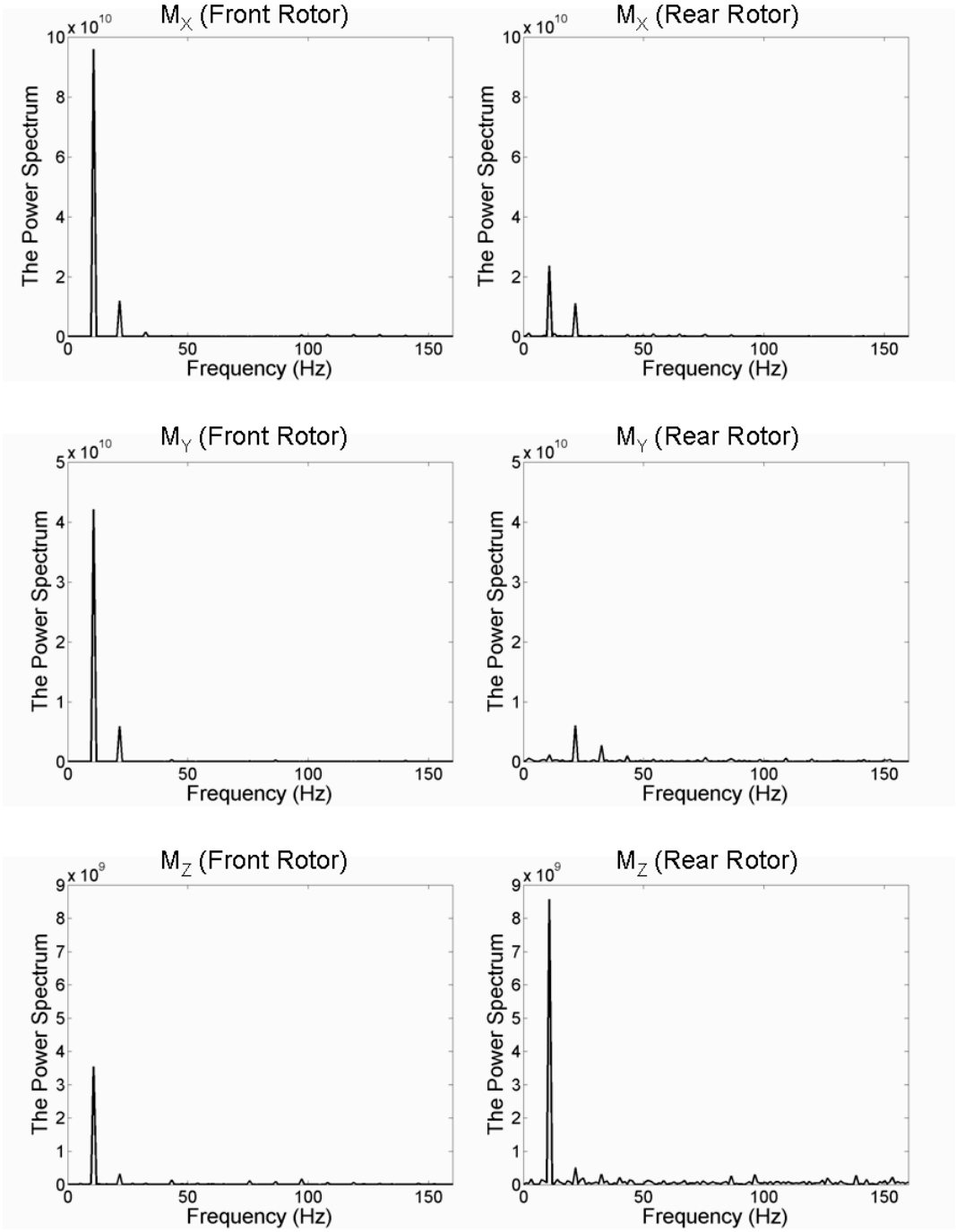

Figure 4.30 *Frequency analysis of moments in case 1c simulation*

Figure 4.31 shows the frequency analysis of F_Z and M_Z in case 1e simulation. Case 1e simulation corresponds to the case when the rear rotor is operating at the advancing side of the front rotor. For the vertical force, both front and rear rotors have a dominant frequency at the blade passing frequency. However, the rear rotor is affected by the

interactions and has bigger peaks at the harmonics. F_X and F_Y have similar characteristics in frequency analysis and have dominant peaks at the blade passing frequencies. M_Z has a dominant peak at the blade passing frequency in both rotors. However, the rear rotor shows bigger peaks at the harmonics when compared to the front rotor. Moreover, the rear rotor has peaks that do not occur in the front.

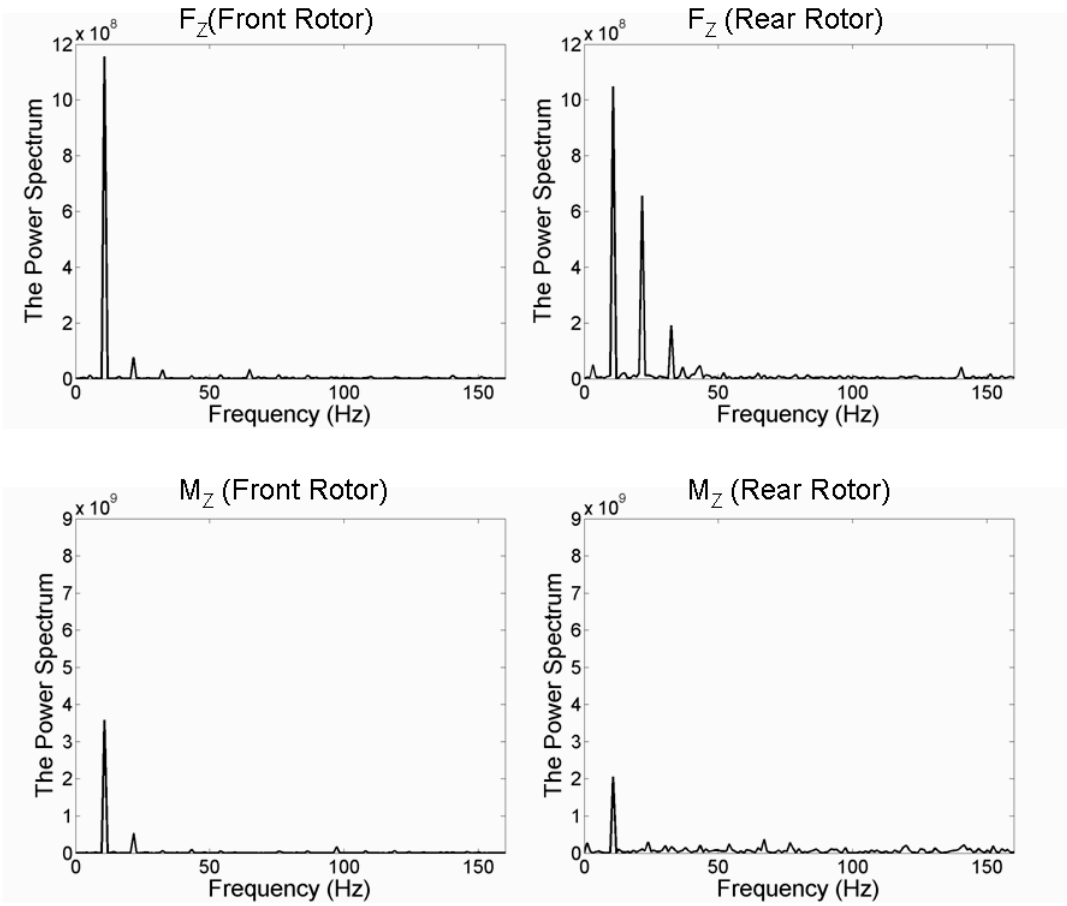

Figure 4.31 *Frequency analysis of F_Z and M_Z in case 1e simulation*

Figure 4.32 shows the frequency analysis of $F_{Z,}$ M_Y and M_Z in case 1a simulation. Case 1a simulation corresponds to the case when the rear rotor is operating at the retreating side of the front rotor. Because of the interactions with the front rotor wake, the dominant frequency of the vertical force of the rear rotor occurs at 21.6 Hz. Similarly, the pitching moment of the rear rotor has a dominant frequency at 21.6 Hz. Yawing moments of both rotors have a dominant frequency at the blade passing frequencies.

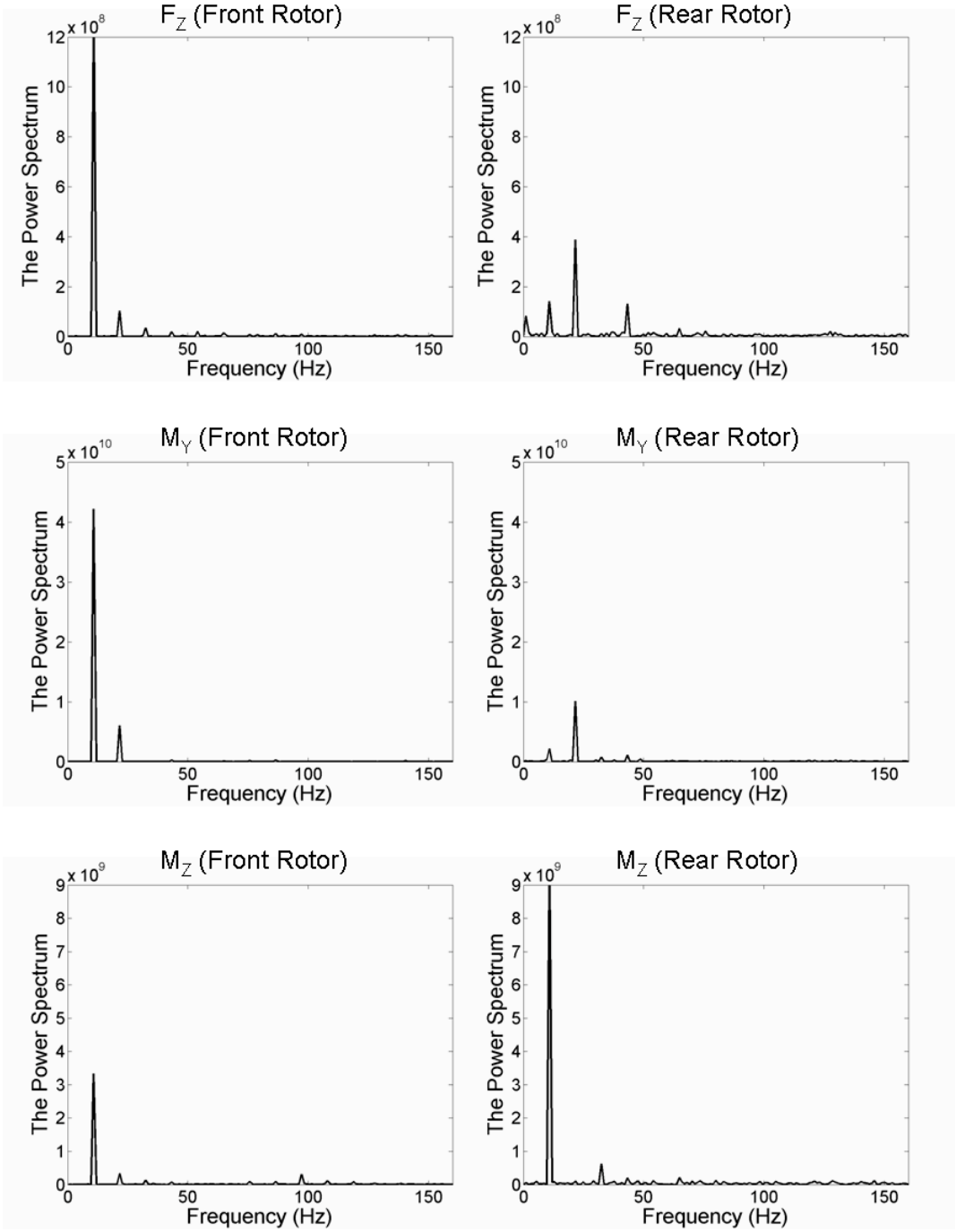

Figure 4.32 *Frequency analysis of F_Z, M_Y and M_Z in case 1a simulation*

CHAPTER 5

CONCLUSIONS

Numerical simulations of helicopter rotor flow fields are a challenging task due to the complex and unsteady nature of the flow field. The main rotor wake interacts with the tail rotor, empennage and the airframe. These interactions alter the induced velocity field and may cause undesirable consequences in performance and handling qualities of the helicopter. The interactions with the presence of a second rotor cause extremely complex and highly unsteady flow field and therefore different wake geometries are obtained.

In this thesis, the capabilities of a new aerodynamic analysis tool, AeroSIM+, have been examined. AeroSIM+ is a 3-D unsteady vortex panel method potential flow solver using free vortex wake methodology. AeroSIM+ is validated for hovering Caradonna-Tung rotor. It was observed that the aerodynamic loading is sensitive to changes in vortex core size. The purpose of this study is to gain a better understanding of the complex flow field in forward flight generated by interaction of two rotors, one operating in the wake of other. The motivation of this study is that the computed forces and moments and the results of their frequency analysis can be implemented in helicopter flight dynamics simulators.

The rotor dynamics were implemented to the AeroSIM+ code in order to account for trim in forward flight. The blade flapping equations were extended to include the additional terms arising from pitching and rolling motions of the helicopter and the shaft tilt angle. The asymmetries in the wake geometry in forward flight cause changes in performance characteristics of the rear rotor when it is operating at port and starboard sides of the front rotor. The decrease in vertical lifting is more when the rear rotor is operating at the starboard side. BVI locations are shown to be different in different forward speeds. Moreover BVI locations are different depending on the relative position of the rear rotor. The mutual interaction between the individual vortex filaments causes distortion in the wake. This distortion is observed stronger at low speed forward flight

since the tip vortices are closest together for many revolutions. High vorticity region near the blade tips rolls up into a pair of “super-vortices” at the lateral edges of the wake. The super vortices are similar to the vortices trailing at the tips of a fixed wing. The impact of the super vortices is shown to be different for different forward speeds.

For the future work, code should be developed to be efficient in terms of computational time. The flight dynamics trim code should be implemented to the AeroSIM+ code in order to solve the trim equations at each wake iteration.

REFERENCES

[1] Leishman, J. G., Bagai, A., "Challenges in Understanding the Vortex Dynamics of Helicopter Rotor Wakes", AIAA Journal, Vol. 36, No. 7, 1998.

[2] Leishman, J. G., *Principles of Helicopter Aerodynamics*, Cambridge University Press, Newyork, 2002.

[3] Landgrebe, A.J., "The Wake Geometry of a Hovering Helicopter Rotor and its Influence on Rotor Performance", Journal of the American Helicopter Society, Vol. 17, No.4, pp. 3-15, Oct. 1972.

[4] Schmitz, F. H., "Rotor Noise", *Aeroacoustics of flight vehicles: Theory and Practice,* Vol. 1. NASA Reference Publication, Ch. 2, p.1258, August 1991.

[5] McCroskey, W. J., "Vortex Wakes of Rotorcraft" AIAA paper, 95-0530, Aerospace Sciences Meeting and Exhibit, 33rd, Reno, NV, January 1995

[6] Yu, Y. H., "Miss Distance for Blade-Vortex Interaction Noise reduction", AIAA Paper No. 96-1738, Second AIAA/CEAS Aeroacoustics Conference, State College, PA, May 1996

[7] Schmitz, F. H., and Yu, Y. H., "Helicopter Impulsive Noise: Theoretical and Computational Status", Journal of Sound and Vibration, Vol. 109, No. 3, pp. 361-422, 1986.

[8] Rahier, G., and Delrieux Y., "Blade-Vortex Interaction Noise Prediction Using a Rotor Wake Roll-Up model", Journal of Aircraft, Vol. 34, No. 4, pp. 522, July-August 1997.

[9] Yu Y. H., Gmelin B., Splettstoesser W, Philippe J. J, Prieur J, Brooks T. F., "Reduction of helicopter blade-vortex interaction noise by active rotor control technology" Progress in Aerospace Sciences, Vol. 33, No.9, pp. 647-687, 1997.

[10] Bi, N., Leishman, J. G., and Crouse, G. L., "Investigation of Rotor Wake Interactions with a Body in low Speed Forward Flight", AIAA-91-3228-CP, presented at the AIAA 9th Applied Aerodynamics Conference, Baltimore, MD, Sept. 23-26, 1991.

[11] Bi, N., and Leishman, J. G., "Experimental Study of Rotor/Body Aerodynamic Interactions", Journal of AAircraft, Vol. 27, No. 9, September 1990.

[12] Brand, A. G., McMahon, H. M., and Komerath, N. M., "Surface Pressure Measurements on a Body Subject to Vortex Wake Interaction" AIAA Journal, Vo. 27, No.5, pp.569, May 1989.

[13] Prouty, R. W., "*Helicopter Performance, Stability, and Control*", PWS Publishers, Boston, MA, 1986.

[14] Pegg, R.,J., and Shidler, P.,A., "Explanatory Wind Tunnel Investigation of the Effect of the Main Rotor Wake on Tail Rotor Noise" Presented at the AHS/NASA/Army Specialists Meeting on Helicopter Acoustics, Hampton, Virginia, NASA CP 2052, May 1978.

[15] Bagai, A., and Leishman, J. G., "Free-Wake Analysis of Tandem, Tilt-Rotor and Coaxial Rotor Configurations," Journal of the American Helicopter Society, Vol.41, No. 3, July 1996, pp.196-207.

[16] Airliners,http://www.airliners.net/photo/Russia---Army/Kamov-Ka-50/0812591/&sid=8af54e0ac42a94aa0ee20cc2a14378ae , last accessed date : 8/12/2009

[17] Airliners,http://www.airliners.net/photo/UK---Air/Boeing-Chinook-HC2/1566642/&sid=4b2d9fb4649e710e32d8ab8526cd104e , last accessed date : 8/12/2009

[18] Nasa, http://www.dfrc.nasa.gov/gallery/photo/XV-15/HTML/EC80-13848.html, last accessed date : 8/12/2009

[19] Wilson, J. C., and Mineck, R.E., "Wind –Tunnel Investigation of Helicopter Rotor Wake Effects on Three Helicopter Fuselage Models" NASA Report TM X-3185,1975.

[20] Sheridan, P. F., and Smith R. P., “Interactional Aerodynamics- A New Challenge to helicopter Technology”, Journal of American Helicopter Society, Vol. 25, No. 1, pp. 3-21, January 1980.

[21] Smith, C. A., and Betzina, M.D., “Aerodynamic Loads Induced by a Rotor on a Body of Revolution” Journal of the American Helicopter Society, Vol. 31, No. 1, 1986.

[22] McMahon, H. M., Komerath, N. M., and Hubbard, J. E., “Studies of Rotor-Airframe Interactions in Forward Flight” AIAA Paper 85-5015, 1985.

[23] Wilby, P. G., Young, C., and Grant, J. “ An Investigation of the Influence of Fuselage flow Field on Rotor Loads and the Effects of Vehicle Configuration”, Vertica, Vol.3, No.2, pp. 79-94, 1979.

[24] Betzina, M. D., Smith, C. A., and Shinoda, P., “Rotor/Body Aerodynamic Interactions” Vertica, ISSN 0360-5450, Vol. 9i o. 1, pp. 65-81, 1985.

[25] Fletcher, T. M., Brown, R. E., “Main rotor – Tail Rotor Wake Interaction and its Implications for Helicopter Directional Control”, Proceedings of the 32nd European Rotorcraft forum, Maastricht, Netherlands, 2006.

[26] Meakin, RL., “Moving Body Overset Grid Methods for complete tilt-rotor simulations”, AIAA Paper 93-3350-CP, Presented at the 11th AIAA Computational Fluid Dynamics Conference, Orlando, FL, July 1993.

[27] Akimov, A. I., Butov, V. P., Bourtsev, B. N., and Selemenev, S. V., “Flight Investigation of Coaxial rotor Tip Vortex Structure”, Proceedings of the American Helicopter Society, Alexandria, VA, pp. 1431-1449, 1994.

[28] Brown, R. E. “Rotor Wake Modeling for Flight Dynamic Simulation of Helicopters” AIAA Journal, Vol. 38, No. 1, January 2000.

[29] Leishman, J. G., Bhagwat, M. J., and Bagai, A., "Free-Vortex Filament Methods for the analysis of Helicopter Rotor Wakes", Journal of Aircraft, Vol. 39., No. 5, 2002, pp. 759-775

[30] Dumitrescu, H., Frunzulica, F., "A Free Wake Aerodynamic Model for Helicopter Rotors", Proceedings of the Romanian Academy, Series A, Vol. 5, No. 3/2004.

[31] Szymendera C.J., "Computational Free Wake Analysis of a Helicopter Rotor", Mater of Science, Pennsylvania Sate University, May 2002.

[32] Katz, J. and Plotkin, A., "*Low – Speed Aerodynamics"*, 2nd Ed. Cambridge University press, 2000.

[33] Sezer-Uzol, N., "High-Accuracy Wake and Vortex Simulations using aHybrid Euler/Discrete Vortex Method", Mater of Science, Pennsylvania Sate University, May 2001.

[34] Caradonna, F. X. and Tung, C., Experimental and Analytical Studies of a Model Helicopter Rotor in Hover, NASA TM-81232, 1981.

[35] Katz, J. and Maskew, B., "Unsteady Low-Speed Aerodynamic Model for Complete Aircraft Configurations" Journal of Aircraft, Vol.25, No.4, pp. 302-310, April 1988.

[36] Tarımcı, O., Yılmaz, D., and Yavrucuk I., "On the Level of Center of Gravity Modeling Error in Neural Network based Adaptive Controller Design", 2008.

[37] Johnson W., "*Helicopter Theory*", Princeton University Press, Princeton, N. J., 1980.